

Reduction of fibrillar strain-rate sensitivity in steroid-induced osteoporosis linked to changes in mineralized fibrillar nanostructure

L. Xi^{*a,b}, P. De Falco^{*b,c}, E. Barbieri^{b,d}, A. Karunaratne^e, L. Bentley^f, C.T. Esapa^{f,g}, G.R. Davis^m, N.J. Terrill^h, R.D. Cox^f, N. M. Pugno^{j,b,k}, R.V. Thakker^g, R. Weinkamer^c, W.W. Wu^{a,#}, D.N. Fang^{a,l} and H.S. Gupta^{b,#}

a. Institute of Advanced Structure Technology, Beijing Institute of Technology, Beijing 100081, China

b. School of Engineering and Material Sciences, Queen Mary University of London, London, E1 4NS, UK

c. Department of Biomaterials, Max Planck Institute of Colloids and Interfaces, D-14424 Potsdam-Golm, Germany

d. Department of Mathematical Science and Advanced Technology (MAT), Yokohama Institute for Earth Sciences (YES) 3173-25, Showa-machi, Kanazawa-ku, Yokohama-city, Japan

e. Department of Mechanical Engineering, University of Moratuwa, Sri Lanka

f. MRC Mammalian Genetics Unit and Mary Lyon Centre, MRC Harwell, Harwell Science and Innovation Campus, OX11 0RD, UK

g. Academic Endocrine Unit, Radcliffe Department of Clinical Medicine, Oxford Centre for Diabetes, Endocrinology and Metabolism (OCDEM), University of Oxford, Churchill Hospital, Headington, Oxford, OX3 7JL, UK

h. Beamline I22, Diamond Light Source Ltd., Diamond House, Harwell Science and Innovation Campus, Chilton, Didcot, Oxfordshire, OX11 0DE, United Kingdom

j. Laboratory of Bio-Inspired & Graphene Nanomechanics, Department of Civil, Environmental and Mechanical Engineering, University of Trento, Via Mesiano, 77, 38123, Trento, Italy

k. Ket Lab, Edoardo Amaldi Foundation, Via del Politecnico snc, 00133, Rome, Italy

l. State Key Laboratory for Turbulence and Complex Systems, College of Engineering, Peking University, Beijing, China

m. Dental Physical Sciences Unit, Queen Mary University of London, London, E1 4NS, UK

*. These authors contributed equally to this work.

#. Correspondence authors

E-mail addresses: xili@bit.edu.cn (L. Xi), paolino.defalco@mpikg.mpg.de (P. De Falco),

e.barbieri@jamstec.go.jp (E. Barbieri), angelok@uom.lk (A. Karunaratne), l.bentley@har.mrc.ac.uk (L.

Bentley), c.esapa@har.mrc.ac.uk (C.T. Esapa), g.r.davis@qmul.ac.uk (G.R. Davis),

nick.terrill@diamond.ac.uk (N.J. Terrill), r.cox@har.mrc.ac.uk (R.D. Cox), nicola.pugno@unitn.it (N. M.

Pugno), rajesh.thakker@ndm.ox.ac.uk (R.V. Thakker), richard.weinkamer@mpikg.mpg.de (R.

Weinkamer), wuwenwang@bit.edu.cn (W.W. Wu), fangdn@bit.edu.cn (D.N. Fang), h.gupta@qmul.ac.uk

(H.S. Gupta).

#Correspondence author:

Himadri S. Gupta, h.gupta@qmul.ac.uk

School of Engineering and Materials Sciences and Institute of Bioengineering,

Queen Mary University of London, Mile End Road, London E1 4NS, UK

Tel: +44(0)20 7882 8867

Wenwang Wu, wuwenwang@bit.edu.cn

Institute of Advanced Structure Technology, Beijing Institute of Technology

Beijing 100081, China

44 **Significance Statement**

45 Biomechanically bone undergoes different loading-rates, from low (standing) to high (rapid loading
46 during fracture), and its mechanical response varies with strain-rate. However, the role of the
47 mineralized fibrillar matrix in contributing to the change in mechanical response is incompletely
48 understood. In particular, the changes in bone matrix strain-rate sensitivity during metabolic bone
49 disorders like osteoporosis are little studied. Here, we use rapid synchrotron X-ray imaging during
50 variable strain-rate tests on cortical bone from a murine model of steroid-induced osteoporosis, to
51 study the matrix-level response. We find that while control-samples showed an increase in effective
52 fibrillar and mineral modulus with strain-rate, this effect is completely suppressed in osteoporotic bone.
53 We model this effect by considering the matrix as a two-level fibrillar/lamellar composite, and find
54 that the changes may be explained by an altered interaction between the collagen and mineral at the
55 nanoscale. Our results suggest that an altered strain-rate sensitivity of the bone matrix in osteoporosis
56 may be one of the contributing factors to reduced mechanical competence in such metabolic bone
57 disorders.

58

59

60 **Abstract**

61 As bone is used in a dynamic mechanical environment, understanding the structural origins of its time-
62 dependent mechanical behaviour – and the alterations in metabolic bone disease – is of interest.
63 However, at the scale of the mineralized fibrillar matrix (nanometre-level), the nature of the strain-rate
64 dependent mechanics is incompletely understood. Here, we investigate the fibrillar- and mineral-
65 deformation behaviour in a murine model of **Cushing's syndrome, used to understand** steroid induced
66 osteoporosis, using synchrotron small- and wide-angle scattering/diffraction combined with *in situ*
67 tensile testing **at three strain rates ranging from** 10^{-4} to 10^{-1} s⁻¹. We find that the effective fibril- and
68 mineral-modulus and fibrillar-reorientation show no significant increase with strain-rate in
69 osteoporotic bone, but increase significantly in normal (wild-type) bone. By applying a fibril-lamellar
70 two-level structural model of bone matrix deformation to fit the results, we obtain indications that
71 altered collagen-mineral interactions at the nanoscale – along with altered fibrillar orientation
72 distributions – may be the underlying reason for this altered strain-rate sensitivity. Our results suggest
73 that an altered strain-rate sensitivity of the bone matrix in osteoporosis may be one of the contributing
74 factors to reduced mechanical competence in such metabolic bone disorders, and that increasing this
75 sensitivity may improve biomechanical performance.

76

77 **1 Introduction**

78 Determining the mechanically-critical structural and compositional alterations of bone matrix in
79 metabolic bone disorders, such as osteoporosis or osteogenesis imperfecta, is essential to understand
80 origins of the reduced mechanical competence exhibited in such disorders [1-3]. A systematic
81 characterization of the mechanical properties of bone **was** pioneered by John Currey [4]. Among his
82 many contributions to biomechanics, he found that stiffness, strength and toughness of bone depend
83 on biological factors such as anatomical specialisation [5] and species [6], as well as on factors related
84 to materials-composition and structure, such as mineral [7] and collagen content [8, 9]. The research
85 presented here was performed in the spirit of his systematic approach, but focusses not on quasi-static
86 mechanical properties, but on changes of the mechanical performance under **three** different loading
87 speeds. As bone is used under time-dependent loading in a dynamic mechanical environment, linking
88 the viscoelastic and strain-rate dependent behaviour of bone matrix to such alterations is important.
89 However, clinical measures assessing bone state (such as bone mineral density (BMD)) capture mainly
90 changes in bone mass, and provide little information on alterations in quality of the bone matrix. The
91 matrix of bone at the nanoscale is a composite of Type-I collagen fibrils, carbonated apatite,
92 noncollageneous proteins and water [10, 11], which are assembled into fibre-arrays at the micron-
93 scale[12, 13] **and** further aggregate into trabecular and cortical bone types to form the organ bone [5].
94 Metabolic bone diseases may affect not only the macro- and microscale structure of bone, but also
95 change the bone matrix-level quality [2], via altered cellular modelling and remodelling cycles.
96 Alterations in matrix quality, such as collagen-cross linking [8, 9, 14] mineral-platelet structural
97 changes [15] and the expression of noncollageneous proteins like osteopontin [16], have been shown
98 to lead to deterioration or alteration in macroscopic mechanical properties, but the details of the
99 nanoscale mechanisms are not completely understood. Understanding the nanostructural response of
100 bone matrix to time-dependent loading in bone-disease types like osteoporosis is therefore of
101 importance both to basic medical science as well as, eventually, to clinical practice.

102 In this regard, glucocorticoid induced osteoporosis (GIOP) is a prototypical secondary osteoporosis
103 where BMD is known to be insufficient to explain mechanical changes. As the most common form of
104 secondary osteoporosis, GIOP affects 1-3% of the general population and results in severe morbidity,
105 especially in post-menopausal women and older men [17, 18]. GIOP usually develops in patients
106 receiving glucocorticoids for the treatment of a variety of diseases like inflammatory and autoimmune
107 disorders, and these underlying diseases themselves can also have negative effects on bone metabolism
108 which constitute a risk of osteoporosis [19]. Glucocorticoids treatment results in altered bone
109 remodelling, early and rapid bone loss and increased fracture risk, through direct effects on bone cells

110 and indirect effects through alteration of the neuromuscular system and gonadal hormones [20]. As a
111 crucial process in GIOP, reduced bone volume is caused by osteoclastic activity (bone resorption) that
112 cannot be matched by osteoblastic activity (bone formation) [21, 22]. Glucocorticoids suppress
113 bone formation through inducing osteoblast and osteocyte apoptosis and the inhibition of proliferation,
114 differentiation, maturation and activity of osteoblasts [23]. In the presence of glucocorticoids, the
115 osteoblast precursor cells (mesenchymal cells) in bone marrow are not differentiated or directed toward
116 osteoblastogenesis, but toward adipogenesis (cells of the adipocytic lineage) [24]. Glucocorticoids
117 inhibit the differentiation of osteoblasts by a mechanism of opposing *Wnt*/ β -catenin pathway, and *Wnt*
118 signalling plays a critical role in increasing bone mass through induction of differentiation of bone-
119 forming cells (osteoblasts), inhibition of osteoblast and osteocyte apoptosis, and suppression of the
120 development of bone-resorbing cells (osteoclasts) [25, 26]. Glucocorticoids directly affect osteoclasts
121 resulting in decreased osteoclast apoptosis and increased osteoclast formation of a prolonged life span,
122 which explains the observed enhanced and prolonged bone resorption [27]. The proliferation of
123 osteoclasts is inhibited by glucocorticoids in a dose dependent manner. Although excess of
124 glucocorticoids leads to an increased osteoclast number, osteoclast function may be affected too, with
125 impaired spreading and resorption of mineralized matrix. The osteoblast signals could also be impaired
126 due to the abnormal osteoclast function [28].

127 However, the way these biological changes in GIOP affect the nano- and microscale mechanics is
128 incompletely understood, especially in the area of time-dependent loading. Previous studies have
129 showed that glucocorticoid therapy affects not only the amount of bone (bone quantity) but also the
130 micro-architecture and other material level properties (bone quality) [17, 29, 30]. Micro-CT studies of
131 trabecular and cortical bone with glucocorticoids treatment showed reduced trabecular bone volume,
132 trabecular connectivity, trabecular number and cortical thickness as compared to control group [31,
133 32]. Glucocorticoid-treated mice showed increased size of osteocyte lacunae and there are “halos” of
134 hypomineralized bone surrounding the lacunae, with corresponding reduced (~40%) mineral to matrix
135 ratio as measured by Raman microspectroscopy. A reduction in mineral concentration (by 45%) caused
136 by glucocorticoids treatment is accompanied by reduced degree of bone mineralization, as compared
137 to controls [31]. Our previous study on a mouse model of endogenous hypercorticozonaemia
138 (Cushing's syndrome) shows a significant reduction (by 51%) of fibril modulus, larger fibril
139 strain/tissue strain ratio and a disruption of intracortical architecture as compared with their wild-type
140 littermates [33]. In relation to mechanics, bone fractures in healthy individuals usually happen with
141 traumatic events at high strain rates, whereas in GIOP, bones are additionally involving fragility
142 fractures with minimal trauma at relatively low strain rates [1, 34, 35]. Since the quasi-static fibrillar-

143 level mechanics and structure are altered in GIOP-bone [15, 33], it is therefore of interest to investigate,
144 in this prototypical secondary osteoporosis, possible viscoelastic and strain-rate dependent effects in
145 the mineralized fibrillar matrix.

146 In this study, we **examine** the deformation of the mineralized fibrils in the bone matrix of a GIOP
147 mouse model **at three different strain rates**, using high-brilliance time-resolved synchrotron small-
148 angle X-ray scattering (SAXS) and wide-angle X-ray diffraction (WAXD). These X-ray techniques
149 provide information on the fibrillar- and mineral platelet-level strain in the bone matrix, induced by
150 external mechanical loads. When combined with a high brilliance synchrotron source, SAXS/WAXD
151 measurements can be carried out with time-resolution of the order of seconds [14, 15, 36-38],
152 facilitating dynamic measurements. For the animal model of GIOP, we use a mouse model ($Crh^{-120/+}$)
153 of endogenous hypercorticonaemia (Cushing's syndrome), published as a model of endogenous
154 GIOP [39]. **Prior work has suggested that fracture risk in endogenous glucocorticoid production**
155 **(Cushing's syndrome) is similar to that in exogenous GIOP [40], although we acknowledge of the**
156 **limitation of using mouse models to understand human GIOP, due to the absence of secondary osteonal**
157 **remodelling.** Our previous quasi-static (not time-dependent) SAXS/WAXD study, on the
158 developmental changes in bone nanostructure in this model, provided evidence for increased fibrillar
159 deformability, more random fibrillar orientation, and shorter/less stress-reinforcing mineral platelets
160 in GIOP [15, 33]. Here, we carry out tensile deformation on cortical GIOP mouse bone at a fixed age
161 point (24 weeks) and **at three strain rates to** quantify the alterations in fibrillar mechanics in comparison
162 to wild-type animals. Because SAXS/WAXD measurements are intrinsically volume-averaged
163 measures of nanoscale deformation, the experimental data is combined with a multiscale model of the
164 mechanics of the fibrils and fibril-arrays, developed from previous work [13, 36, 41], to help in the
165 interpretation of the experimental results.

166 **2 Materials and Methods**

167 **2.1 Animals**

168 Bone tissue from female GIOP mice ($Crh^{-120/+}$) and wild-type ($Crh^{+/+}$) littermates on a C57BL/6
169 genetic background (3rd generation) aged 24 weeks were used in this study. Mouse samples were stored
170 at $-20\text{ }^{\circ}\text{C}$ before experiments. The mice were bred as part of a prior study [39], where all animal studies
171 were carried out using guidelines issued by the UK Medical Research Council, in Responsibility in
172 Use of Animals for Medical Research (July 1993) and Home Office Project License numbers 30/2433
173 and 30/2642.

174 **2.2 Sample preparation for *in situ* tensile testing**

175 Murine femora were dissected and longitudinally sectioned along the long axis using a water-irrigated
176 low speed saw with a diamond-coated blade. The distal and proximal ends of anterior femora strips
177 were embedded in dental ionomer (Filtek™ Supreme XT, 3M ESPE, USA) such that samples could
178 be mounted in the microtensile tester. The dental ionomer was exposed in UV light for 20 s, while the
179 mid-diaphysis of femora bone was covered by lead tap during UV light exposure to prevent any UV-
180 induced tissue alteration. The obtained femora strips for microtensile testing have typical gauge length,
181 width and thickness of 5 mm, 1 mm and 0.2 mm, respectively. Samples were then wrapped in PBS-
182 soaked tissue paper and stored at - 20 °C before used for mechanical testing.

183 **2.3 *In situ* micro tensile testing with simultaneous synchrotron SAXD/WAXD measurements**

184 Combining *in situ* tensile testing with real time synchrotron SAXD and WAXD, the load data (from
185 load cell), fibril strain ϵ_f (from the SAXD frames) and mineral strain ϵ_m (from the WAXD frames) can
186 be collected concurrently, as initially devised by Gupta et al. [37]. A customized microtensile tester
187 was mounted in the path of synchrotron X-ray beam at beamline I22, Diamond Light Source (Harwell,
188 UK), such that SAXD and WAXD frames were collected concurrently with mechanical loading of the
189 sample. Samples were uniaxially loaded in tension using a customized microtensile tester equipped
190 with a DC linear-encoder stage (M112.1DG; Physic Instruments, UK) and an 111N model
191 SLC31/00025 tension/compression load cell (RDP Electronics Ltd, UK). A custom LabVIEW based
192 software (LabVIEW 2013, National Instruments, UK) was used to control the microtensile tester and
193 CCD camera. Samples were tested at room temperature and hydrated throughout each experiment in a
194 fluid bath filled with physiological saline (PBS solution).

195 For the three different load rates used in the current study, the motor velocities were set to be 0.1, 0.05
196 and 0.002 mm/s, which corresponding to motor strain rates of 0.02 s⁻¹, 0.01 s⁻¹ and 0.0004 s⁻¹,
197 respectively. Strain rates of 0.02 s⁻¹ and 0.01 s⁻¹ were used because they are in the range of
198 physiological strain rates during walking and running, whereas a strain rate of 0.0004 s⁻¹ representing
199 the quasi-static loading was also examined as strain rates near this magnitude have been used in our
200 previous studies [15, 33, 42, 43]. The numbers of samples tested at strain rate of 0.02 s⁻¹, 0.01 s⁻¹ and
201 0.0004 s⁻¹ were 4, 4 and 4, respectively, for wild-type mice; and 6, 5 and 4, respectively, for GIOP
202 mice.

203 For the synchrotron SAXD and WAXD measurement, the X-ray wavelength λ was 0.8857 Å and beam
204 cross section was ~240 × 80 μm at the sample. A Pilatus P3-2M detector was used to collect the SAXD
205 data, while a Pilatus P3-2M-DLS-L detector was used to collect the WAXD data; both detectors have
206 a pixel resolution of 1475 x 1679 pixels and pixel size of 172 x 172 μm². Note that in the concurrent

207 SAXD/WAXD measurement protocol used, one quadrant (lower right) of the WAXD detector space
208 is removed to allow for the remaining SAXD signal to transmit to the downstream SAXD detector; as
209 a result, the WAXD pattern spans 3 out of 4 quadrants on the detector. The sample-to-detector distance
210 was ~ 3727.0 mm for SAXD detector and ~ 175.3 mm for WAXD detector, as measured with Silver
211 Behenate and Silicon standard, respectively. The X-ray exposure time was 0.1 s for both SAXD and
212 WAXD patterns for samples measured at all strain rates. Due to the different durations of the
213 mechanical tests at different strain-rates, the period between successive SAXD/WAXD acquisitions
214 (with beam shutter closed) was controlled by the wait-time parameter (0.1 s: strain rate 0.01 s⁻¹ and
215 0.02 s⁻¹, and 3.4 s: strain rate of 0.0004 s⁻¹). The beam shutter was closed between consecutive
216 acquisitions of SAXD and WAXD patterns, to minimise the effect of X-ray irradiation on the
217 mechanical properties of bone tissue [44].

218 **2.4 SAXD and WAXD data analysis**

219 Fibril strains and load-induced changes in fibrillar orientation distribution were measured from 2D
220 SAXD patterns, and mineral strains were measured from 2D WAXD patterns.

221 **Fibril strain:** The meridional stagger (D-period) of collagen molecules inside the fibril leads to an
222 axial diffraction pattern in the small-angle region of reciprocal space [45]. The third-order meridional
223 collagen reflections were used to measure the D-period of collagen fibrils evaluating a radially-narrow
224 semi-circular sector (180° angular width) (**Figure 1G**); this corresponds to considering an integrated
225 averaged of fibrillar deformation in all directions. The fibril strain (ϵ_f) was calculated from the
226 percentage increases in D-period during tensile testing of samples [15, 33, 45, 46]. SAXD patterns at
227 different stress levels are shown in the *supplementary information* (**Figure S1**).

228 **Mineral strain:** For WAXD, the mineral particles consist of apatite (with a lattice structure of
229 hexagonal closed-packed or *hcp* type) with the *c*-axis predominantly oriented along the fibril direction
230 [47]. In a similar manner to the SAXD analysis, the mineral strain (ϵ_m) along the loading direction was
231 measured from the percentage changes of lattice spacing, obtained from the (002) peak centre position
232 of apatite averaged in a radially-narrow semi-circular (180° angular width) in the upper quadrant, in
233 an analogous manner to SAXD (**Figure 1E**), similar to prior work [14, 15, 38, 45].

234 The *Processing* perspective of the data analysis software package DAWN [48] (www.dawnsci.org)
235 was used for SAXD and WAXD data reduction. The integrated SAXD and WAXD 1D intensity
236 profiles (**Figure 1F and H**) were obtained from 2D SAXS/WAXD images as described above.
237 Subsequently, the 1D profiles were fitted using a custom Python script. Both the 1D collagen SAXD

238 data and the 1D mineral WAXD data were fitted to combinations of a Gaussian peak and a linear
239 background term. To analyse the change of fibril and mineral strains during tensile loading, the
240 obtained peak centre positions were used to calculate the D-period for the collagen fibrils and the (002)
241 crystallographic lattice spacing for the mineral apatite. Linear regressions of D-period and D(002) were
242 carried out versus macroscopic stress, and the intercept of each regression was taken as the unstrained
243 (zero-stress) value for D-period and D(002). The collagen fibril strains ε_f and mineral strains ε_m were
244 calculated from the percentage changes of collagen D-period and the (002) lattice spacing, respectively,
245 relative to the unstrained state. The *effective fibril modulus* ($E_f = d\sigma/d\varepsilon_f$) and *effective mineral modulus*
246 ($E_m = d\sigma/d\varepsilon_m$) were defined as the slope of tissue-level stress σ versus fibril strain and mineral strain,
247 respectively, from the elastic region of deformation (**Figure S3-4, supplementary information**), as
248 described in prior work [15, 33, 45]. We note that the terminology (effective fibril modulus and mineral
249 modulus) is used for consistency with prior work [15, 33, 49], and as will be discussed in the modelling
250 section, these parameters are not equivalent to the actual fibril and mineral elastic modulus (hence the
251 use of the qualifier “effective”).

252 ***Fibrillar orientation distribution:*** The changes in fibrillar orientation distribution with tensile load
253 were analysed by observing the narrowing of the FWHM of the angular variation of SAXD intensity
254 of the first-order collagen reflection, as described in our prior study on quasi-static deformation of
255 glucocorticoid-induced osteoporotic bone [33]. Using the DAWN processing perspective, radially
256 averaged azimuthal intensity profiles $I(\chi; q_0)$ were calculated over the full azimuthal range (360°) from
257 the first-order collagen reflection (at $q = q_0 = 6\pi/D$). To subtract out the diffuse scattering background
258 due to the mineral, similar azimuthal intensity profiles $I_m(\chi; q_0 - \Delta q)$ and $I_m(\chi; q_0 + \Delta q)$ near the first-
259 order collagen reflection, with $\Delta q = 0.015 \text{ nm}^{-1}$ chosen to have $q_0 \pm \Delta q$ outside of the first-order collagen
260 peak, were calculated and averaged. The corrected azimuthal intensity profile $I_c(\chi)$ was calculated as
261 $I_c(\chi) = I(\chi; q_0) - 0.5 \times [I_m(\chi; q_0 - \Delta q) + I_m(\chi; q_0 + \Delta q)]$. The obtained $I_c(\chi)$ was fitted with a pair of
262 Gaussian peak functions separated by 180° . From the fit, the peak position indicates the predominant
263 direction of fibril orientation, while the peak width (FWHM) is related to the extent of fibrillar
264 alignment: larger FWHMs correspond to lower alignment (See **Figure S2** in the *supplementary*
265 *information*). The rate of fibrillar reorientation was calculated from the slope of FWHM (degrees)
266 versus fibril strain (%) curve for each sample [33], with units of degrees/%.

267 **2.5 X-ray microtomography**

268 X-ray microtomography was used to study 3D micromorphometry and microscale mineralization
269 distribution of bone tissue. Mice femora were longitudinally sectioned into two halves. Five samples

270 from both wild-type and GIOP mice were used for X-ray microtomography measurements to obtain
271 tomograms, which were used for quantitative analysis of microscale mineralization distribution in
272 femoral mid-shaft from both wild-type and GIOP mice. Samples were mounted on the sample stage
273 of a high-definition X-ray microtomography scanner (MuCat scanner) which equipped with an
274 ultrafocus X-ray generator (Nikon Metrology (Leuven, Belgium)) and CCD camera (Spectral
275 Instruments Inc (Tucson, Arizona, USA)) in a time-delay integration readout mode. An accelerating
276 voltage of 40 kV was used to scan mice femora samples and a voxel size of $15 \times 15 \times 15 \mu\text{m}^3$ was
277 obtained. The projection data were processed following a calibration procedure, in which the scanning
278 data were corrected to an equivalence of 25 keV monochromatic X-ray source, and then a
279 reconstruction procedure in which a cone-beam back-projection algorithm was used to generate 3D
280 images (representing the absolute linear attenuation coefficient at 25 keV) of the scanned regions of
281 samples. The 3D tomograms of samples were processed with an in-house software (Tomview,
282 authored by GRD) to export a series of 8-bit grey level slices, multiplying the linear attenuation
283 coefficient by a known constant to obtain an appropriate dynamic range. The histograms of grey levels
284 for wild-type mice and two distinct regions of interest in GIOP mice - periosteal region and endosteal
285 region (**Figure 2 C1**)- were generated from 2D slices using ImageJ software (ImageJ, NIH, USA). The
286 histograms of grey levels for three data groups were converted into histograms of mineral
287 concentration using published X-ray attenuation data [50], from which the average mineral
288 concentrations (denoted as the degree of mineralisation) measured as hydroxyapatite (g/cm^3) were
289 calculated and plotted for different bone regions (**Figure 2E-F**). The mineral concentration is
290 converted to mineral volume fraction as previously described [51, 52]. For input of experimental
291 mineral concentrations into the model (described below), the mineral concentration and volume
292 fraction are taken as the average values across the cross-section of the tissue, similar to our prior work
293 [15].

294 **2.6 Calculation of microscale porosity and stress**

295 The experimental stress data was calculated by the load values divided by the area of the fracture
296 surface, and then corrected by the porosity of bone, following our previous study [15]. SEM image
297 was taken on the fracture surface while the fractured sample was mounted vertically, and the area of
298 the fracture surface was measured from SEM image using ImageJ (NIH, Bethesda, USA). The
299 experimental stress data were post-multiplied by the coefficient $1/(1 - p^{3/2})$ to incorporate the effects –
300 on the effective cross-sectional area – of a 3D isotropic distribution of internal porosity in bone [15].
301 In this case the 3D porosity is $p^{3/2}$, where p is the 2D porosity coefficient ($p = 2\text{D area of voids} / 2\text{D}$
302 bone cross section area), as analysed from backscattered electron (BSE) imaging of the cross section

303 of femoral mid-diaphysis of wild-type and GIOP bone, following our earlier work (Supplementary
304 Information in [15]).

305 **2.7 Statistical analysis**

306 To test for statistical differences in bone mineralization and the nanoscale mechanical deformation
307 behaviour between samples tested at three different strain-rates, one-way ANOVA tests with all
308 pairwise multiple comparison procedures (Holm-Sidak method) were performed on the experimental
309 measured results including the mean mineral concentration, the effective fibril modulus, the effective
310 mineral modulus and the fibrillar reorientation rate. SigmaPlot (Systat Software Inc., USA) was used
311 for the statistical analysis. The statistical significances were denoted on the figures (*: $p < 0.05$, **: p
312 < 0.01 , ***: $p < 0.001$, ns: not significant for $p > 0.05$).

313 **2.8 Modelling of fibrillar and lamellar mechanics**

314 To understand the structural mechanisms underpinning trends in E_f , E_m and fibrillar reorientation with
315 strain-rate, we develop a two-level hierarchical model of the fibrils and fibril arrays, based on prior
316 work, which is briefly summarized below (details in Supplementary Information). Analytical fitting
317 (performed in *Matlab* [53]) and numerical (finite element) simulations performed in *Abaqus 6.14* [54]
318 are used to fit the model to data. The experimental parameters are fitted to equivalent model parameters,
319 summarized in the two columns of **Table 1**.

320

321 **Table 1: Description of the moduli introduced for the study of the bone mechanical properties at**
 322 **different length scales and of the fibrillar reorientation phenomenon.** The term ‘effective’ indicates
 323 that the moduli result from the ratio of terms computed at different length scales. Specifically, they are
 324 calculated from the ratio of stresses applied at the macroscale and of strains computed at the
 325 microscale (effective fibril modulus) and at the nanoscale (effective mineral modulus). The equations
 326 used for the analytical calculation of these parameters are listed in Supplementary Information,
 327 Equations S1-S6. ‘afs’ is the average fibril strain, φ_{EM} is the volume fraction of the extrafibrillar matrix
 328 and k is a factor defined in Equation S6.

Nomenclature of the modulus	Experimental	Analytical/Numerical
Effective fibril modulus	$\frac{\text{Applied tissue stress}}{\text{average fibril strain}}$ Calculated via linear fitting of experimental data shown in Figure 5A .	$\frac{\text{Applied laminate stress}}{\text{average strain of the sublamellae}}$ Computed via laminate theory.
Effective mineral modulus	$\frac{\text{Applied tissue stress}}{\text{mineral strain}}$ Calculated via linear fitting of experimental data shown in Figure 5B .	$\frac{\text{Applied tissue stress}}{(afs * \varphi_{EM}) + (afs * \frac{(1 - \varphi_{EM})}{k})}$ Computed via laminate theory.
ΔFWHM/fibril strain	<p>ΔFWHM: variation of the FWHM of Gaussian fitting ‘I vs χ’ curves (more details in Supplementary Information).</p> <p>Fibril strain: average fibril strain, averaged from the volume of bone (beam size * sample thickness) measured by x-ray.</p>	<p>ΔFWHM: variation of the FWHM of the lamellar angular distribution (Gaussian distribution). The fibrillar reorientation leading to this variation was computed via FE simulations.</p> <p>Fibril strain: average strain of the sub-lamellae (computed via laminate theory).</p>

329

330

331 2.9 Model structure and parameters

332 2.9.1 Analytical relations

333 *Nanoscale force-balance relations*: Stresses and strains on the fibril, mineral platelet and extrafibrillar
334 matrix were calculated by considering the fibril as a staggered array of mineral particles embedded
335 with a collagen matrix (**Figure 3A-I**), which is in turn embedded in an extrafibrillar matrix. The model
336 follows earlier work on staggered model architecture of the mineralized fibrils in bone and related
337 biomineralized tissues [11, 36, 41, 55-57]. The mineral platelet aspect ratio was taken as 15 and 9.6
338 respectively for the wild-type and GIOP models, following our prior ultrastructural determination of
339 mineral structure (L -parameter) using WAXD on GIOP- and WT-bone from the same cohort at a
340 similar age-point [15]. A second parameter of note in the staggered model is the k -factor, which is
341 inversely related to the stress transferred to the mineral via shear in the collagen matrix [11, 36].
342 Mineral and collagen were taken as elastic, and the strain-rate sensitivity was incorporated into the
343 material response of the extrafibrillar matrix, whose constitutive law was taken as the Ramberg-
344 Osgood law $\varepsilon = \sigma / (c \dot{\varepsilon}^d)$ [58, 59]. Most parameters were obtained from referenced literature (**Table**
345 **2**), with the exception of the Young's modulus and volume fraction of the extrafibrillar matrix, and the
346 k -factor, which are obtained from nonlinear fitting to the experimental data (**Figure S6**) and will be
347 reported in the **Results**. The tissue mineral volume fraction values were taken from the 24-week time-
348 point values of volume fraction in GIOP- and WT-mice, in our recent work [15], with $\varphi_m = 0.40$ for
349 GIOP and $\varphi_m = 0.45$ for WT.

350 *Plywood structural parameters*: The bone lamella was modelled as a set of differently oriented fibril
351 layers, with angular orientations at 0° , $\pm 5^\circ$, $\pm 10^\circ$, $\pm 15^\circ$, $\pm 30^\circ$, $\pm 45^\circ$, $\pm 60^\circ$, $\pm 75^\circ$ and 90° . To
352 determine the relative thicknesses of each layer, these were varied till the FWHM of the simulated
353 fibril orientation distribution matched the experimental azimuthal intensity distribution of the
354 meridional collagen SAXD peak (**Figure S2**), in a manner similar to our previous work [15]. Details
355 are provided in **Supplementary Information**.

356 *Matching to experimental data*: Least-squares minimizations was carried out by simultaneously fitting
357 the experimental E_f and E_m data to the model expressions (**Figure 5** and **Figure S6** in **Supplementary**
358 **Information**). Each fitted experimental point (at a given strain rate) was weighted by the inverse of
359 its squared standard deviation [60]. The weighted fitting process was performed in *Matlab* with the
360 function *Nlinfit* [53] (**Table 1** and implementation in **Supplementary Information**). **Table 2** describes
361 the choice of the input parameters for the model.

362 **2.9.2 Finite element simulations of fibrillar and lamellar reorientation**

363 To simulate the load-induced reorientation of fibrils toward the loading axis, an approximate method
364 was used, based on finite element simulations. The reorientation of a fibril embedded in an
365 extrafibrillar matrix was determined (**Figure 3B**), assuming isotropic material properties (**Table S2**),
366 by applying a uniform traction of 10 MPa to the top edge of the fibril and calculating angular
367 reorientation from the horizontal and longitudinal displacements. Details are provided in
368 **Supplementary Information.**

369

370

371 **Table 2: Elastic material properties of the basic components and their volume fractions in the Wild**
 372 **and GIOP models at low, medium and high strain rate values. Red: values extrapolated from**
 373 **referenced literature; Blue (with light blue background): values obtained from the fitting process;**
 374 **Black with dark grey background: values that were assumed. The k-factor is linked to the**
 375 **reinforcement of the collagen fibrils by the mineral platelets (Eqns. S2 and S6 in Supplementary**
 376 **Information).**

<i>Young's moduli</i>	GIOP bone (GPa)				Wild-type bone (GPa)	
E_c = Young's modulus of collagen	2.5 [36]				2.5 [36]	
E_m = Young's modulus of hydroxyapatite (mineral content)	100 [36]				100 [36]	
E_{EM} = Young's modulus of extrafibrillar matrix		$k = 1.58$	$k = 1.6$	$k = 1.7$		Extrafibrillar matrix
	low s.r.	163.8	107.6	53.0	low s.r.	3.5
	medium s.r.	160.8	105.7	52.3	medium s.r.	159.0
	high	160.1	105.3	52.1	high	370.0
<i>Poisson's ratios</i>						
ν_c = Poisson's ratio of collagen	0.3 [61]				0.3 [61]	
ν_m = Poisson's ratio of hydroxyapatite (mineral content)	0.28 [61]				0.28 [61]	
ν_{EM} = Poisson's ratio of extrafibrillar matrix	0.3 [61]				0.3	
<i>Volume fractions</i>						
ϕ_c = volume fraction of collagen	0.6				0.55	
ϕ_m = volume fraction of hydroxyapatite (mineral content)		$k = 1.58$	$k = 1.6$	$k = 1.7$	0.45 - $\phi_{EM} = 0.37$	
		0.37	0.34	0.27		
ϕ_{EM} = volume fraction of extrafibrillar matrix		$k = 1.58$	$k = 1.6$	$k = 1.7$	0.08 (from fitting)	
		0.03	0.06	0.13		

377

378

379 3 Experimental Results and Model Fitting

380 3.1 X-ray Microtomography

381 X-ray microtomography was performed to investigate 3D micromorphometry, microscale
382 mineralization distribution and possible mineralization defects of femora from wild-type and GIOP
383 mice. A series of 8-bit grey level slices were obtained from the 3D tomograms of samples. **Figure 2**
384 showed representative 2D slices for both longitudinal and transverse cross sections of femora from
385 wild-type and GIOP mice. The 2D slices of transverse cross sections of femora, as shown in **Figure**
386 **2A** and **C**, are selected from mid-shaft of mice femora as indicated by red dash lines in **Figure 2 B** and
387 **D**. Clear qualitative differences can be observed in the cortical microstructure of GIOP mice as
388 compare with wild-type mice. Both of the transverse and longitudinal cross sections of femoral from
389 GIOP mice showed a very large fraction of cavities with less mineralized bone tissue near the endosteal
390 cortex, whereas no such cavities were found in the femoral mid-shaft of wild-type mice. The femoral
391 cross section of GIOP mice showed a much thinner cortex compared to wild-type mice. **This is in**
392 **agreement with backscattered electron (BSE) imaging results of the cross section of mice femoral mid-**
393 **diaphysis (as also carried out in [15]), which showed 2D porosity coefficients of 1.68 ± 0.26 % and**
394 **29.57 ± 1.74 % for wild-type and GIOP bone, respectively.**

395 Histograms of degree of mineralisation and the mean mineral concentration of middle shaft femoral
396 bone from wild-type (N=5) and GIOP (N=5) mice were measured using X-ray microtomography.
397 Representative distributions of mineral concentration were plotted for mid-shaft femora from wild-
398 type and GIOP mice (**Figure 2E**). While not clearly visible at the lower-magnification whole-bone CT
399 slices in **Figure 2A-D**, our prior work using backscattered electron microscopy on GIOP vs WT-
400 femora (at similar age-points) showed that the mineralization of the endosteal region is clearly lower
401 than the periosteal region in GIOP, while it is similar across regions in WT [33]. Since two distinct
402 regions of interest: endosteal region surrounded by less mineralized halos, and periosteal region, were
403 observed in GIOP mice (**Figure 2 C, D**)[33], they were used separately for quantitative X-ray
404 microtomography analysis (**Figure 2 inset C1**). The weighted average mineral concentrations (denoted
405 as the degree of mineralisation) measured as hydroxyapatite g/cm^3 were calculated from the frequency
406 distribution of mineral concentration and plotted for different groups (**Figure 2 E-F**). One-way
407 ANOVA test indicated that the mean mineral concentration among three groups were significantly
408 different. The weighted average mineral concentration in wild-type mice is significantly higher than
409 that in GIOP periosteal ($p < 0.01$) and endosteal regions ($p < 0.001$), and it is also significantly higher
410 ($p < 0.01$) in GIOP periosteal regions compared to GIOP endosteal regions (**Figure 2F**). The broad

411 distribution of mineral concentration with a fat tail toward low mineral concentration in GIOP
412 endosteal region indicated a microscale heterogeneous mineralisation.

413 **3.2 *In situ* tensile testing with synchrotron SAXD and WAXD**

414 **SAXD and WAXD patterns:** Representative SAXD and WAXD patterns for femoral mid-shaft of wild-
415 type mice aged 24 weeks are shown in **Figure 1E** and **1G**, and 1D intensity profiles of the third-order
416 collagen reflection and (002) mineral reflections in mice femur mid-diaphysis are shown in **Figure 1F**
417 and **1H**.

418 **Effective fibril moduli:** To compare the fibrillar-deformation in mice femur tested at different strain
419 rates (**Figure 5B** and **Figure 4A, D**), data for samples at each strain rate were combined and plotted
420 (tissue stress vs. nanoscale fibrillar strain) in the elastic deformation region (**Figure 4A, D**), and show
421 differences in the slope (effective fibril modulus $E_f = d\sigma/d\varepsilon_f$). Average effective fibril moduli from
422 each group of samples were plotted as a function of strain rate in **Figure 5B** (pink bars). As strain rate
423 increased from 0.0004 s^{-1} to 0.02 s^{-1} , we observe a significant increase in the effective fibril modulus
424 increased from $13.6 \pm 3.0\text{ S.D. GPa}$ to $65.6 \pm 11.4\text{ S.D. GPa}$ ($p < 0.001$) in wild-type mice bone.

425 In contrast, the effective fibril modulus remains nearly constant in GIOP mice bone (blue bars). The
426 effective fibril modulus in wild-type mice are significantly ($p < 0.001$) higher compared to GIOP mice
427 at strain rates 0.01 and 0.02 s^{-1} , no significant differences in the effective fibril modulus between wild-
428 type and GIOP mice was found at strain rate 0.0004 s^{-1} (**Figure 4** and **Table 3**). Note that for the data
429 plotted in **Figure 5 B-D**, the parameters E_f , E_m and rate of fibrillar reorientation are calculated per-
430 sample and averaged within each strain-rate group, whilst the lines in **Figure 4** are regressions through
431 the pooled data points (tissue stress vs fibril strain, mineral strain or reorientation) from all samples at
432 that strain-rate. This difference accounts for slight differences in the slopes between the Figures: for
433 example, the averaged fibril moduli in GIOP is lowest at the highest strain rate (0.02 s^{-1} ; **Figure 5B**)
434 while the slope of the regression line for GIOP-bone in the fibril moduli plot in **Figure 4D** is lowest
435 for the intermediate strain rate 0.01 s^{-1} .

436 **Effective mineral moduli:** In a parallel manner, considering the mineral crystallite deformation, tissue
437 stress versus mineral strain were grouped and plotted for **three** different strain rates (**Figure 4B, E**).
438 Here, the effective mineral modulus ($E_m = d\sigma/d\varepsilon_m$) in wild-type mice bone increased with strain rate
439 and the increase was significant ($p = 0.026$) as seen in **Figure 5C** (dark blue bars). E_m increased from
440 $44.2 \pm 7.3\text{ S.D. GPa}$ to $97.5 \pm 28.3\text{ S.D. GPa}$ as strain rate increased from 0.0004 s^{-1} to 0.02 s^{-1} in wild-
441 type mice bone. In contrast, E_m remains nearly constant in GIOP mice bone (blue bars). The effective

442 mineral modulus in WT mice were significantly higher compared to GIOP mice at all strain rates
 443 (**Figure 4** and **Table 3**).

444 **Fibrillar reorientation**: Considering the fibrillar orientation with respect to the direction of loading,
 445 the azimuthal intensity distributions of the first-order collagen reflection from mice femur were used
 446 to determine the degree of fibrillar orientation (FWHM) at unstrained state and the change of FWHM
 447 during tensile loading. Wild-type mice bone shows that 1) the FWHM consistently narrows with
 448 increasing strain, but 2) the percentage-change reduces dramatically as the strain rate increases (**Figure**
 449 **4C**). Averaged values of the rate of fibrillar reorientation were plotted as a function of strain rate in
 450 **Figure 5D**, and showed a significant ($p = 0.018$) reduction. In wild-type mice bone, the rate of fibrillar
 451 reorientation (-40.8 ± 23.2 S.D. $^{\circ}.\%^{-1}$) at low strain rate (0.0004 s^{-1}) is significantly higher as compared
 452 to strain rates of 0.01 s^{-1} ($p = 0.034$) and 0.02 s^{-1} ($p = 0.025$).

453 In contrast, for GIOP bone there are no significant differences in reorientation rate with strain rates.
 454 The reorientation rate in GIOP mice bone at strain rate 0.0004 s^{-1} is significantly lower than that in wild-
 455 type bone, whereas no significant differences in reorientation rate was found between wild-type and
 456 GIOP mice bone at strain rate 0.01 s^{-1} and 0.02 s^{-1} (**Figure 4** and **Table 3**).

457 **Table 3**: *Effective fibril moduli, effective mineral moduli and fibrillar reorientation in WT- and GIOP-*
 458 *bone; p-values report differences between WT- and GIOP- in each group.*

	Strain rate (s^{-1})	Wild-type	GIOP	P-value
Effective fibril moduli (GPa)	0.004	13.60 ± 3.00	14.46 ± 2.66	0.876
	0.01	37.90 ± 9.90	13.02 ± 4.28	< 0.001
	0.02	65.60 ± 11.40	11.50 ± 3.58	< 0.001
Effective mineral moduli (GPa)	0.004	44.20 ± 7.29	17.90 ± 5.30	0.032
	0.01	70.50 ± 16.70	20.77 ± 1.42	< 0.001
	0.02	97.49 ± 28.38	26.66 ± 10.50	< 0.001
Reorientation rate (degree / %)	0.004	40.75 ± 23.22	2.18 ± 9.65	< 0.001
	0.01	4.90 ± 3.91	1.76 ± 5.63	0.703
	0.02	5.50 ± 4.94	1.24 ± 4.02	0.606

459

460 3.3 Model fitting to experimental E_f , E_m and reorientation:

461 An initial fitting process for the two models allowed the Young's moduli corresponding to the three
 462 analyzed strain rate values and the volume fraction of the extrafibrillar matrix (**Figure 5A**) to be
 463 calculated. **Figure 5A** shows the variation of the modulus of extrafibrillar matrix. In the wild-type case

464 the extrafibrillar matrix stiffens by over a factor of 100 – from 3.5 GPa at $\dot{\epsilon} = 0.0004 \text{ s}^{-1}$ (low strain
465 rate) to 370.0 GPa at $\dot{\epsilon} = 0.02 \text{ s}^{-1}$ (high strain rate). In the GIOP case, instead, depending on the
466 imposed k -factor and on the strain rate, values of the extrafibrillar Young's modulus can range between
467 52.1 and 163.8 GPa (**Table 2**).

468 **Figure 5B** shows a comparison between the experimental and numerically computed effective fibril
469 modulus E_f . For the wild model, the results show agreement within the experimental error bars,
470 underestimation at medium and high strain rate values and overestimation at the low strain rate ($\dot{\epsilon} =$
471 0.02 s^{-1}). For the wild-type model a stiffening effect with an increasing strain rate – as seen in
472 experiment – was also found at the mineral level (**Figure 5C**). The effective mineral modulus, E_m , is
473 overestimated at high and medium strain rates and slightly underestimate at low strain rate.

474 For the GIOP bone, both the effective fibrillar and mineral moduli confirm the constant trend found
475 experimentally (**Figure 5B-C**) and show agreement with experimental values (average experimental
476 13.6 GPa vs 13.9 GPa). Indeed, the average experimental value of the effective fibril modulus at the 3
477 strain rates is 13.6 GPa while the corresponding modelling value is 13.9 GPa. Corresponding values
478 for the effective mineral modulus are respectively 22.8 GPa and 21.8 GPa.

479 **Figure 5D** shows that for lamellar-level fibrillar reorientation – calculated via change of $\Delta FWHM$
480 normalised by the fibril strain – the wild-type model reproduces the trend to reduced reorientation with
481 increased stress. For the GIOP model a reduction of the k -factor (**Equation S6**) lead to a reduction of
482 fibrillar reorientation (**Figure 5D**). Our parametric analysis shows that the reorientation calculated via
483 FE simulations matches the experimental reorientation (modelling values within the experimental error
484 bars) for 3 strain rates assuming $k = 1.58$.

485

486 4 Discussion

487 Strain-rate dependent tensile tests were performed on small femoral samples of wild-type and
488 steroid-induced osteoporotic (GIOP) mice. Our main findings can be summarized as follows:

- 489 • Under tensile testing with increasing strain rate, the fibrillar-level deformation of GIOP bone
490 exhibits a contrasting behaviour to wild-type (WT; normal) murine bone – specifically, while
491 WT-bone shows a significant increase in effective fibril- and mineral-moduli, this effect is
492 absent in GIOP bone
- 493 • On increasing strain-rate, WT-bone shows a significant reduction of extent of fibrillar
494 reorientation toward the loading axis; in contrast, GIOP bone shows no change in reorientation
495 with strain-rate.
- 496 • By comparing the volume-average SAXS- and WAXD-measures of fibril- and mineral-strain
497 to the model predictions of a fibril/fibril-array model of bone matrix mechanics, the strain-rate
498 dependent effects in WT-bone are explained via an increased extrafibrillar matrix stiffening.
- 499 • In contrast, for GIOP-bone, the experimental results can be matched to model predictions if the
500 reinforcement between mineral- and collagen (via the k -factor; **Table 2**) at the nanoscale is
501 taken higher for GIOP compared to WT, and no extrafibrillar matrix stiffening occurs in GIOP-
502 bone.

503 The novelty of the current study is primarily in obtaining experimental data characterising how the
504 strain-rate dependence of fibrillar deformation mechanics in osteoporotic bone differ from normal
505 cortical bone, and as a secondary goal, to explore the underlying structural mechanism by fitting a
506 multilevel model to the data. Prior work, by our group as well as others [14, 15, 33, 42] have analysed
507 alterations in fibrillar mechanics in metabolic bone disorders like rickets, GIOP, and ageing, but these
508 have not studied strain-rate dependence in such pathological conditions. Because bone is used in a
509 dynamic mechanical environment, understanding how the structural response of the bone matrix at the
510 fibrillar level alters with increasing strain rate is of direct interest. From a materials-standpoint, for
511 example, our observation that the fibril strain gradient (from E_f) is unchanged at different strain rates
512 in GIOP-bone, but decreases in WT-bone (**Figure 4**), provides insight into the altered biomechanical
513 reinforcing efficiency of the collagen fibrils. Further, while the current work does not directly deal
514 with fracture, prior work by other groups has shown that strain-rate influences work of fracture, with
515 reduction of work of fracture and transition to unstable crack growth with increasing strain rate [62,
516 63], as well as increase of elastic moduli and yield strength [64]. Indeed, if fibrils in osteoporotic GIOP
517 bone show no change with increasing strain rate, while an effective “stiffening” is seen via the

518 increased fibril modulus in normal (WT) bone, this may lead to a lower mechanical competence in
519 GIOP at higher strain-rates compared to WT. When compared with the wild-type bone, the relationship
520 between strain rate and increasing modulus breaks down for GIOP, indicating the mineral-collagen
521 composite in GIOP failed to adequately stiffen with increasing strain rate, which is likely the cause of
522 the lowered mechanical competence. While the lower maximal fibril strain in WT relative to GIOP
523 sounds counterintuitive when one associates disease with lowered strength and brittleness, we note
524 that a) the total tissue strain is a complex sum of the fibril, interfibrillar, and interlamellar level strains
525 and b) the maximal elastic stress level in GIOP is lower than WT. Therefore, the expected weak (lower
526 strength) behavior in GIOP is present, whilst the lower maximal fibril strain in WT- does not exclude
527 that the maximal strain at macroscopic failure will still be lower in GIOP than WT (possibly due to
528 tissue-level defects and pores). We note, however, an underlying assumption in our work is that the
529 mouse model of endogenous glucocorticoid production (Cushing's syndrome) is a valid and relevant
530 model for (exogenous) human GIOP [40]. As mouse models do not exhibit secondary remodelling, the
531 bone structure at the tissue level will be different from human GIOP.

532 The strain-rate dependence of the mechanical properties of bone have been studied at the
533 macroscopic level before [58, 64-66], using phenomenological viscoelastic/viscoplastic models or
534 relations such as the Ramberg-Osgood equation used earlier. The nature of the structural mechanisms
535 in time-dependent mechanical loading is less studied. High strain-rate *in situ* SAXD measurements on
536 human bone found a strain-rate induced stiffening of the fibril ductility associated with a loss in
537 toughness in bone matrix [38], and compressive creep studies found the strain on both mineral and
538 collagen phases in bone increase linearly with time, proposed as a load-shedding from collagen to
539 mineral [67]. Stress-relaxation was observed to be more rapid in mineral than in collagen [68].
540 Molecular dynamics studies (e.g. [69]) have highlighted the role of rapidly breaking and reforming
541 hydrogen bonds during deformation. Nevertheless, structural-mechanisms enabling viscoelasticity in
542 the bone matrix are not clearly known, and the experimental data on the variation of the time-dependent
543 behaviour in osteoporosis presented here may help toward that eventual goal. It is noted that the
544 exposure of the samples to X-rays is consistent across three different strain-rates. By closing the shutter
545 between acquisitions, and keeping acquisition time constant at 0.1s per point, the total X-ray dose is
546 proportional to the number of SAXS patterns per tensile test. Figure S5 (Supplementary Information)
547 shows that the number of patterns is of the same order of magnitude across strain-rates. Therefore, it
548 is not likely that the high-strain rate tests are being exposed to much higher X-ray dosages compared
549 to the low- and medium strain-rates, which would cause damage to the collagen matrix [44].

550 The experimental values for maximal fibril strain (**Figure 5A**) at low strain rates ($\sim 0.4\text{-}0.6\%$)
551 are consistent with our prior quasi-static results on both murine [15, 33, 42] and bovine bone [37], and
552 in the same range as those observed by others on human bone [14]. In WT-bone, the maximal fibril
553 strain reduces consistently from $\sim 0.6\%$ at the lowest strain rate (0.0004 s^{-1}) to $\sim 0.1\%$ at the highest
554 strain-rates (0.02 s^{-1}). However, a similar trend is not visible for GIOP; for intermediate strain rates
555 (0.01 s^{-1}) in GIOP-osteoporotic bone – in **Figure 4D**, maximum fibril strain can reach $\sim 0.6\text{-}0.8\%$
556 compared to the $\sim 0.4\%$ values for the lowest strain-rate, while for the highest strain rate the maximum
557 fibril strain is again $\sim 0.4\%$. Since maximum strains are linked to strength and failure of the entire bone,
558 microstructural differences between GIOP- and wild-type bone (**Figure 2**) may be relevant in
559 explaining this behaviour, which is beyond the scope of the nano/microscale model presented and
560 discussed below.

561 Fibrillar reorientation, as well, shows some notable differences between GIOP and WT. Here,
562 it is important to note certain experimental limitations. As SAXD and WAXD provide volume
563 averaged measures of fibrillar/mineral structure through the thickness of cortical bone specimens used
564 in these tests, effects *below* and *above* the scale of the fibril cannot be excluded. Consequently, if the
565 sample volume contained microscopically misaligned lamellae, these could undergo inter-lamellar
566 reorientation, rather than the reorientation occurring at the fibril/interfibrillar matrix alone (this
567 corresponds to phenomena above the scale of the fibril). Likewise, it is known that tropocollagen
568 molecules inside microfibrils are arranged in a tilted geometry [70] and intrafibrillar rearrangement
569 may also contribute, rather than fibrils rotating in a rigid-body manner. **However, we note that the**
570 **numerical value of the tilt inside microfibrils is small ($\sim 4^\circ$ in Figures 2-3 in [70]) (noting the factor of**
571 **5 compression in the c-axis direction specified by the authors). This value is much smaller (**Figure 5D**)**
572 **compared to the $\sim 50^\circ$ (FWHM change)/% strain reorientation seen for the lowest strain rate. Therefore,**
573 **load-induced intrafibrillar rotation of the molecules, to remove the tilt, would be insufficient to explain**
574 **the magnitude of the observed reduction in FWHM. To be able to overcome the averaging issue**
575 **inherent in our experimental configuration, possible future routes may involve 6D SAXS tensor**
576 **tomography [71], if challenges in data processing and potential radiation damage are overcome. Such**
577 **methods can provide spatially-resolved 3D maps of the fibrillar nanostructure across the tissue,**
578 **although time-resolved studies at the strain-rates proposed here (and above) will still be challenging.**
579 **Subfibrillar-level deformation may be analysed by the covariation of changes in the angular intensities**
580 **of the WAXD and SAXS patterns (which will provide information on how the mineral particles are**
581 **reorienting relative to the fibrils), or possibly by contrast-variation neutron diffraction to resolve the**
582 **changes in tropocollagen ordering.**

583 While the empirical differences between the strain-rate dependencies in the GIOP- and WT-
584 nanoscale parameters (E_f and E_m) is clear from **Figures 4-5**, these numbers (averaged across scattering
585 volume) by themselves do not provide a full structural explanation. From our earlier studies on GIOP-
586 bone [15, 33], the orientation distribution is wider in GIOP than WT. These facts imply that earlier
587 simpler models, such as our prior work on antler [36], which modelled the uniaxial fibrils alone
588 (oriented along the loading axis), are likely insufficient to explain the data. As a first step in this
589 direction, we used a two-level multiscale model of bone nano- and microstructure to provide some
590 insights into possible reasons for these changes. At the fibrillar level, the model is similar to prior
591 staggered models of mineral-collagen interactions put forward [11, 36, 41, 55-57, 61, 72], although
592 the inclusion of the mechanics of the extrafibrillar matrix is an advance on our prior modelling [36].
593 At the fibril-array level (microscale), bone is known to have a lamellar structure although the precise
594 details of the orientation (originally proposed as plywood or rotated plywood [13, 73]) are still not
595 fully clear, with recent revisions to the orientation scheme proposed [12] to incorporate a fraction (10%)
596 of disordered fibrils. The plywood scheme used in the original paper [13] is used here (also for
597 consistency with prior modelling work [61]), but inclusion of more complex structures to model the
598 experimental results is possible in the future. Further, the microstructure of rat and mice bone is
599 different from human bone, which has extensive secondary remodelling and well developed secondary
600 osteons, and these differences are not accounted for in the model. In addition, spatial variations in bone
601 matrix parameters at larger length scales than the nano- and micro- (such as across cross-sections of
602 cortical bone reported in rat bone [74]) are beyond the scope of the model, even though clear variations
603 between endosteal and periosteal regions (**Figure 2**) are visible. Parameter estimates from the model
604 and their structural interpretation below need therefore to be considered as estimates rather than
605 definitive values.

606 From optimizing the parameters for model predictions to agree with experimental values of
607 effective fibril- and mineral-moduli, it is observed that in normal WT cortical bone the stiffening of
608 the extrafibrillar matrix with increasing strain-rate can lead to the increased fibril (and mineral)
609 modulus seen experimentally (**Figure 5**). Increased stress borne by the extrafibrillar matrix reduces
610 the strain on the fibrils, which therefore increases the effective fibril modulus, which is a ratio of
611 macroscopic stress to fibril strain. A similar process occurs for effective mineral moduli. The
612 extrafibrillar space in bone contains extrafibrillar mineral and non-collagenous proteins [75, 76], and
613 we can speculate that such a phase of mineral interlinked with protein may exhibit strain-stiffening
614 behaviour with increasing strain-rate, being dominated by the moduli of the noncollagenous proteins
615 (< 1 GPa) at low strain rates and by the modulus of the mineral at larger strain rates. However, we

616 obtain unrealistically high values for the modulus of the extrafibrillar matrix (370 GPa) at the highest
617 strain rate, well above the 100-110 GPa characteristic of hydroxyapatite mineral [36]. Possibly, these
618 values arise from the extrafibrillar volume fraction or type of orientation distribution used here, and
619 parametric-variation studies may be useful in future in this regard.

620 In contrast, the experimental data for the GIOP-bone can be fit to the model with essentially
621 constant extrafibrillar matrix moduli (**Table 2**) but with a considerably lowered k -factor. The physical
622 meaning of this difference compared to WT bone is not fully clear. The k -factor is inversely linked to
623 the reinforcing efficiency of the mineral platelets inside the collagen fibril [11, 36], and arises due to
624 the load-transfer from the collagen matrix to the mineral platelet. Note that the effect of the more
625 random fibril orientation in GIOP [15, 33] has already been included via the wider FWHM from $I(\chi)$.
626 As the k -factor depends on the effectiveness with which loads are transferred to the mineral from the
627 collagen, the differing k -factor in GIOP compared to WT suggests that possibly the orientation and/or
628 interactions of intrafibrillar mineral with collagen may differ. However, this still does not explain why
629 we do not obtain a similar strain-rate dependent stiffening as seen in WT-bone. We can speculate that
630 these open questions are linked to limitations of our model. As the fibril orientation distribution is not
631 precisely the multilayer lamellar structure described initially [13] but includes random fibril
632 orientations [12], and the further differences in lamellar structure in GIOP have not yet been
633 determined, it is likely that further alterations or refinements to the structural model will be needed,
634 even though the experimental differences between GIOP- and WT-bone fibrillar strain-rate
635 dependencies are not in question.

636 A limitation of the current work is that we did not report results of varying the collagen- and
637 mineral-moduli in the model, both of which may change in disease due to substitution of ions and
638 change in covalent crosslinking [14, 77]. In this regard, we have observed (data not shown) that
639 variation of collagen moduli cannot explain the increase in effective mineral moduli (**Figure 5C**) with
640 strain rate. Regarding the mineral phase, our previous study [15] showed that, compared to WT bone,
641 the mineral platelet is slightly shorter (in length, along the c-axis) and the intra-platelet lattice spacing
642 is slightly higher in GIOP bone, but the mechanical implications of these crystallographic changes is
643 not clear to us at this point. Perhaps, future *ab initio* molecular dynamics simulations of the change in
644 mineral crystallite structure [78], linked to simulated mechanical testing at these small scales, could
645 shed light on this question.

646 In summary, we have analysed for the first time the fibrillar- and mineral-level strain changes
647 in steroid-induced osteoporotic and normal murine bone with increasing strain-rate, and have found

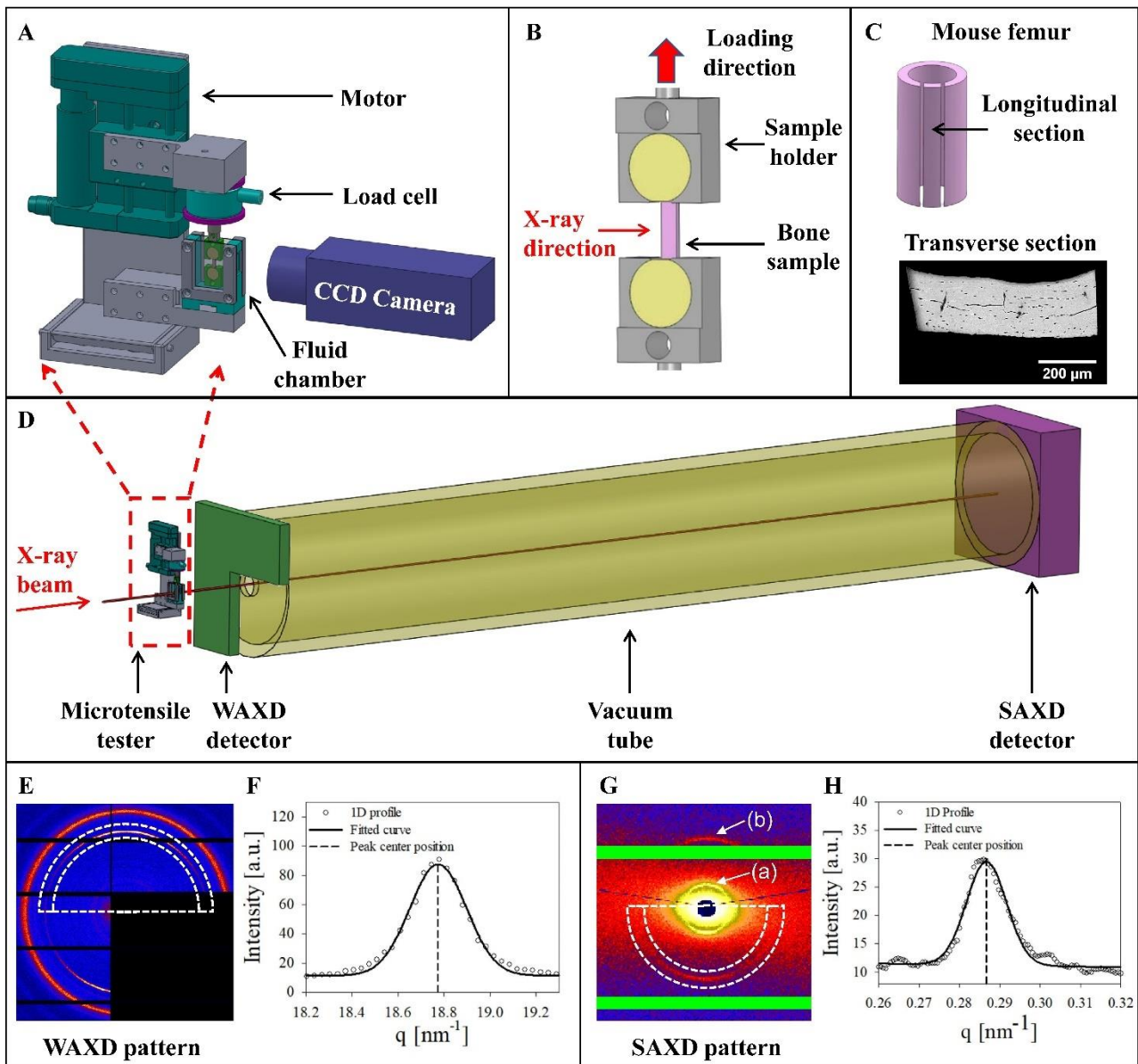
648 both a) clear changes with strain-rate for normal bone and b) a near constant-response across strain-
649 rates for osteoporotic bone. Modelling the bone matrix as arrays of mineralized fibrils with intervening
650 matrix, our results suggest alterations in extrafibrillar matrix stiffness and mineral-collagen
651 reinforcement factors may be the underlying factors. Our results provide insight into the time-
652 dependent nature of fibrillar mechanics in both normal and osteoporotic bone, and may be relevant in
653 understanding the structural origins (in terms of bone quality) of the lower mechanical competence in
654 osteoporosis.

655 **Acknowledgments**

656 This work was supported by Diamond Light Source (Harwell, UK), Queen Mary University of London
657 (grant no. SEML1B4R), the Medical Research Council UK (grant no. G0600702) and the National
658 Science and Technology Major Project (2017-V I -0020-0093). L.X. is supported by the China
659 Scholarship Council (CSC). NMP is supported by the European Commission with the Graphene
660 Flagship Core 2 n. 785219 (WP14 “Composites”) and FET Proactive “Neurofibres” n. 732344 as well
661 as by the MIUR with the “Departments of Excellence” grant L. 232/2016, ARS01-01384-PROSCAN
662 Grant and the PRIN-20177TTP3S. We thank Diamond Light Source (Harwell, UK) for the award of
663 synchrotron beamtime to carry out the *in situ* SAXD/WAXD experiments (SM9893, SM11806, and
664 SM12483). HSG acknowledges support from BBSRC (BB/R003610/1) and from UKRI
665 (MR/R025673/1).

666

667

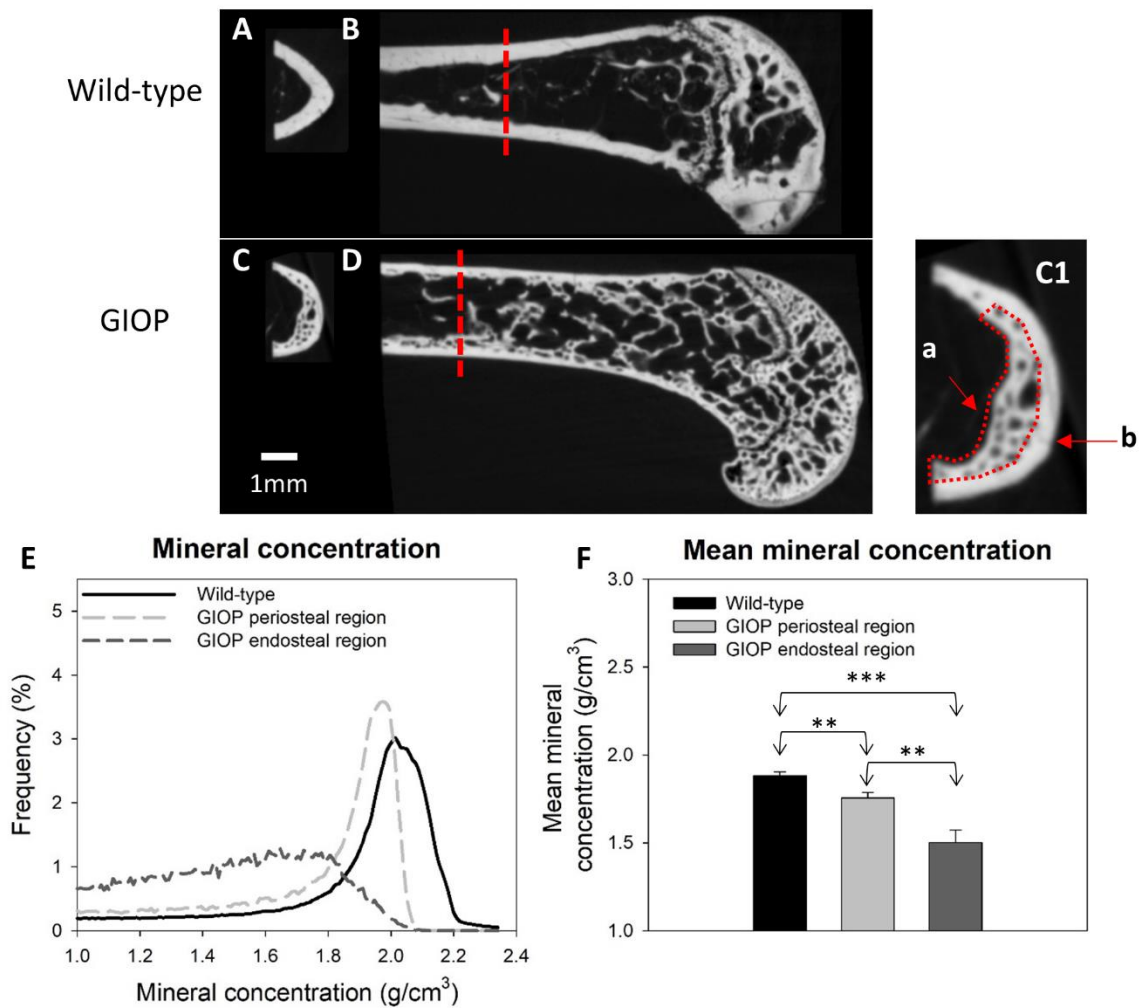


669

670 **Figure 1: In situ nanomechanics with simultaneous synchrotron SAXD and WAXD.** (A) Customized
 671 tensile tester with bone sample mounted in a fluid chamber. (B) Magnified view of sample and tensile
 672 grips in fluid chamber, with tensile strain along the vertical direction. (C) Upper: Schematic of mouse
 673 femur, with tensile test specimen sectioned along the long axis of femur; lower: backscattered electron
 674 image of transverse section of specimen. (D) Experimental configuration: Tensile tester with specimen
 675 mounted along the X-ray beam path in transmission geometry; an L-shape WAXD detector, vacuum
 676 tube and SAXD detector were positioned along the X-ray beam path. (E) 2D WAXD pattern from bone
 677 apatite with predominant c-axis orientation vertical. Dotted lines denote the 180° region for azimuthal
 678 averaging of intensity around the (002) peak of apatite. (F) Azimuthally averaged radial intensity
 679 profile $I(q)$ for the pattern in E. (G) 2D SAXD pattern from collagen fibrils in bone with predominant
 680 fibril orientation vertical. Dotted lines denote the 180° region over which the collagen reflection is
 681 averaged azimuthally; (a) the first-order and (b) the third-order collagen reflection. (H) Azimuthally

682 *averaged radial intensity profile $I(q)$ for the pattern in G. For F and H, black solid line: peak fit with*
683 *a Gaussian function plus a linear baseline; black dashed line: peak centre position.*

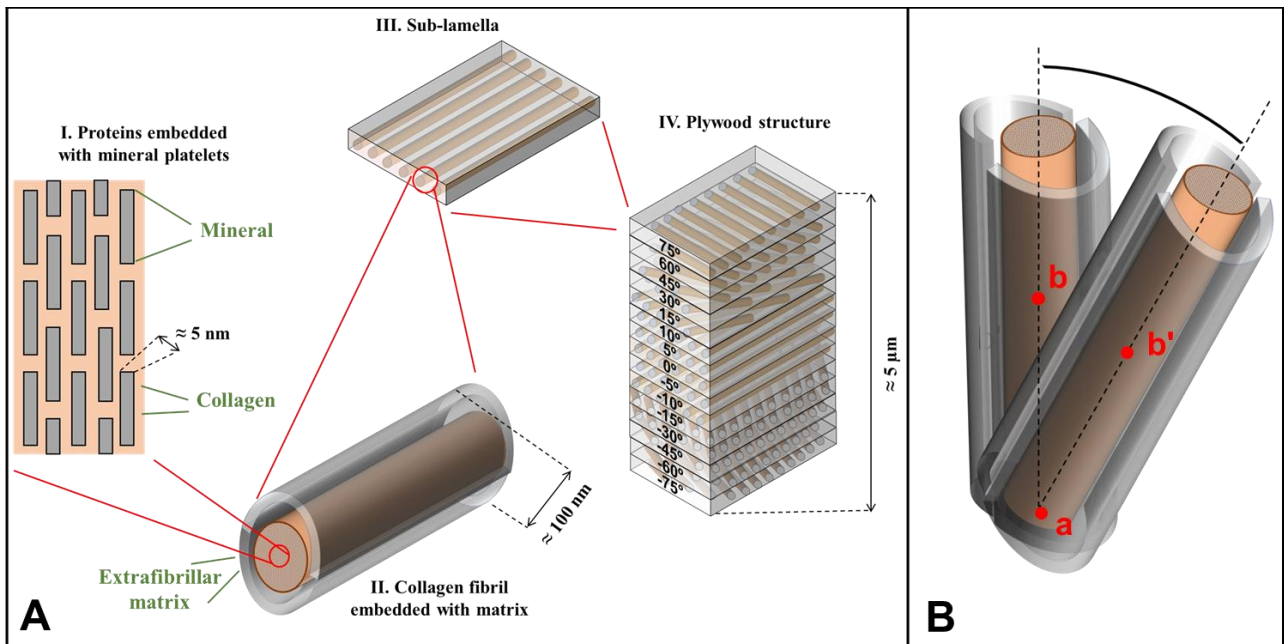
684



686

687 **Figure 2: X-ray microtomography and degree of mineralisation.** Representative 2D slices from X-
 688 ray microtomography measurement for both transverse (A, C) and longitudinal (B, D) cross sections
 689 of femora from wild-type and GIOP mice. Red dash line indicated location where the 2D slice of
 690 transverse cross section was taken. C1: Inset on right shows an example 2D transverse slice, with (a)
 691 indicating the endosteal region and (b) the periosteal region. (E) Representative histograms of degree
 692 of mineralisation were plotted for wild-type (black), GIOP periosteal regions (light gray) and GIOP
 693 endosteal regions (dark gray). (F) Bar chart of the mean mineral concentration for wild-type cortex,
 694 GIOP periosteal regions and GIOP endosteal regions. Error bars shown are standard deviations.
 695 Statistical significances were denoted on the figures (* $p < 0.05$, ** $p < 0.01$, *** $p < 0.001$, ns: not
 696 significant).

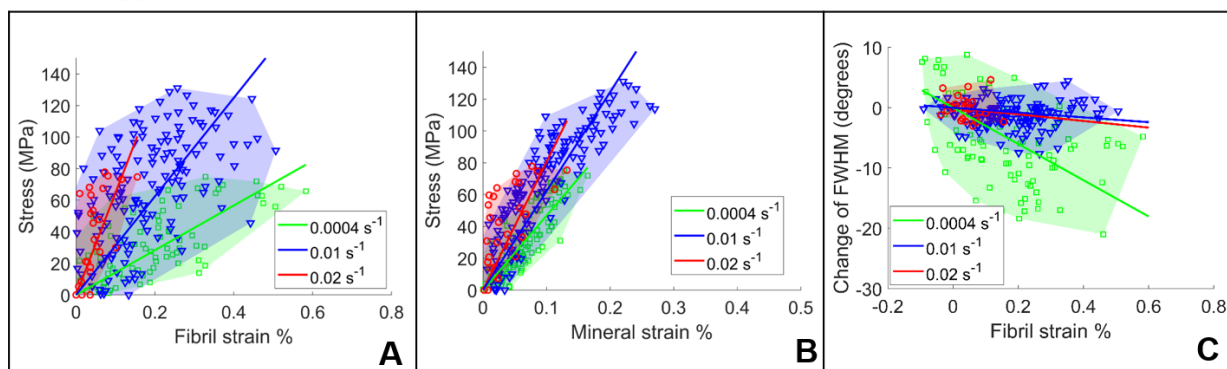
697



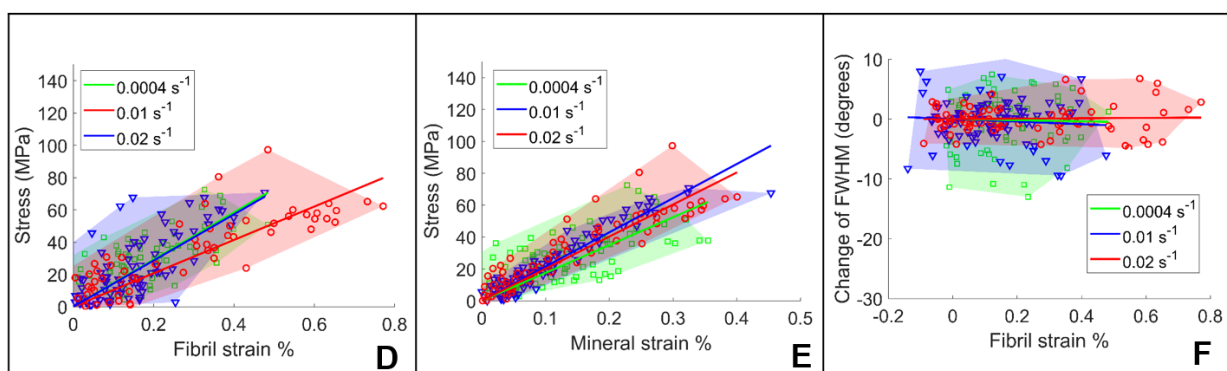
698

699 **Figure 3: Schematic of the hierarchical structure of bone assumed for the modelling approach.** A)
 700 I. At the lowest hierarchical scale, a staggered arrangement of hydroxyapatite mineral platelets and
 701 collagen [41] (left side of the figure) was considered. The material components are collagen,
 702 hydroxyapatite mineral and extrafibrillar matrix (which together form level II). A bunch of parallel
 703 collagen fibrils surrounded by an extrafibrillar matrix, forming a sublamella (III). A set of sub-
 704 lamellae, each with the longitudinal axis of fibrils pointing toward a specific direction, forms (IV) a
 705 plywood (or Bouligand [79]) system. For both modelling approaches the scheme in [13] with an
 706 angular distribution of sub-lamellae of the type: 0° , $\pm 5^\circ$, $\pm 10^\circ$, $\pm 15^\circ$, $\pm 30^\circ$, $\pm 45^\circ$, $\pm 60^\circ$, \pm
 707 75° , (0° direction is along the applied loads). B) Schematic for reorientation in the model.

Wild-type



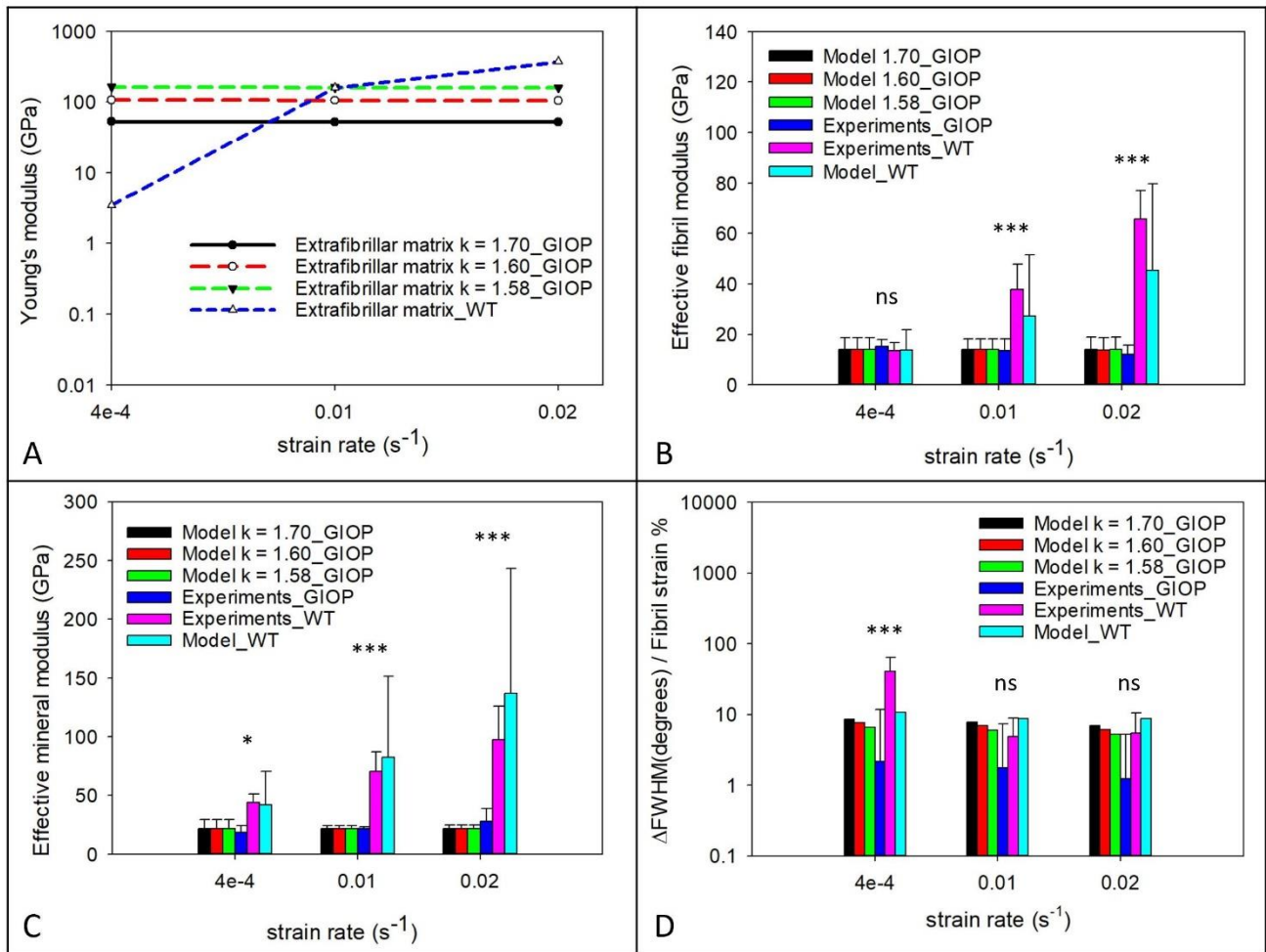
GIOP



708

709 **Figure 4: Fibril strain, mineral strain and change of FWHM from in situ synchrotron SAXD and**
 710 **WAXD:** Symbol code: Low strain rate (0.0004 s⁻¹, green squares), medium strain rate (0.01 s⁻¹, blue
 711 triangles) and high strain rate (0.02 s⁻¹, red circles). (A, D) Applied tissue stress vs average fibril
 712 strain. (B, E) Applied tissue stress vs average mineral strain. (C, F) Change of the FWHM of a
 713 Gaussian profile vs average fibril strain (see also text and **Table 1** for parameter definitions). The
 714 symbols are experimental data points (pooled across samples for each strain rate) while the straight
 715 lines are linear regression lines for each group of data (regressions through pooled data points at a
 716 given strain-rate). The shadowed area in the six plots is a convex hull of the experimental data
 717 representing the region that numerical results are expected to intersect.

718



719

720 **Figure 5: Nanoscale structural parameters of bone mineral and fibrils from experiments and**
 721 **modelling:** (A) Young's modulus of collagen and extrafibrillar matrix at different strain rates from
 722 simulation results (in log scale). (B) Effective fibril modulus, (C) effective mineral modulus and (D)
 723 reorientation rate (in log scale) are plotted as a function of strain-rate. Error bars shown are standard
 724 deviations for experimental data while are 95% confidence interval from the fitting process. One-way
 725 ANOVA tests were performed to test for statistical differences in the experimental results of the
 726 effective fibril modulus, the effective mineral modulus and the fibrillar reorientation rate between
 727 samples tested at different strain-rates. Statistical significance is denoted (* $p < 0.05$, ** $p < 0.01$, *** p
 728 < 0.001 , ns: not significant).

729

730 **References**

731 **Uncategorized References**

- 732 [1] J.A. Kanis, Diagnosis of osteoporosis and assessment of fracture risk, *The Lancet* 359(9321) (2002) 1929-
733 1936.
- 734 [2] E. Seeman, P.D. Delmas, Bone quality--the material and structural basis of bone strength and fragility,
735 *The New England journal of medicine* 354(21) (2006) 2250-61.
- 736 [3] A. Carriero, E.A. Zimmermann, A. Paluszny, S.Y. Tang, H. Bale, B. Busse, T. Alliston, G. Kazakia, R.O.
737 Ritchie, S.J. Shefelbine, How Tough Is Brittle Bone? Investigating Osteogenesis Imperfecta in Mouse Bone, *J*
738 *Bone Miner Res* 29(6) (2014) 1392-1401.
- 739 [4] J.D. Currey, The structure and mechanics of bone, *Journal of Materials Science* 47(1) (2012) 41-54.
- 740 [5] J. Currey, *Bones: Structure and Mechanics*, Princeton University Press 2002.
- 741 [6] J.D. Currey, Mechanical properties of vertebrate hard tissues, *Proceedings of the Institution of*
742 *Mechanical Engineers. Part H - Journal of Engineering in Medicine* 212(H6) (1998) 399-411.
- 743 [7] J.D. Currey, Effects of Strain Rate, Reconstruction and Mineral Content on Some Mechanical-Properties of
744 Bovine Bone, *Journal of Biomechanics* 8(1) (1975) 81-86.
- 745 [8] J.D. Currey, Role of collagen and other organics in the mechanical properties of bone, *Osteoporosis Int* 14
746 (2003) S29-S36.
- 747 [9] P. Zioupos, J.D. Currey, A.J. Hamer, The role of collagen in the declining mechanical properties of aging
748 human cortical bone, *Journal of Biomedical Materials Research* 45(2) (1999) 108-116.
- 749 [10] S. Weiner, H.D. Wagner, The material bone: Structure mechanical function relations, *Annual Review of*
750 *Materials Science* 28 (1998) 271-298.
- 751 [11] P. Fratzl, R. Weinkamer, Nature's hierarchical materials, *Progress in Materials Science* 52(8) (2007)
752 1263-1334.
- 753 [12] N. Reznikov, R. Shahar, S. Weiner, Bone hierarchical structure in three dimensions, *Acta Biomater* 10(9)
754 (2014) 3815-3826.
- 755 [13] S. Weiner, W. Traub, H.D. Wagner, Lamellar bone: structure--function relations, *Journal of structural*
756 *biology* 126(3) (1999) 241-255.
- 757 [14] E.A. Zimmermann, E. Schaible, H. Bale, H.D. Barth, S.Y. Tang, P. Reichert, B. Busse, T. Alliston, J.W. Ager,
758 R.O. Ritchie, Age-related changes in the plasticity and toughness of human cortical bone at multiple length
759 scales, *Proceedings of the National Academy of Sciences* 108(35) (2011) 14416-14421.
- 760 [15] L. Xi, P. De Falco, E. Barbieri, A. Karunaratne, L. Bentley, C.T. Esapa, N.J. Terrill, S.D.M. Brown, R.D. Cox,
761 G.R. Davis, N.M. Pugno, R.V. Thakker, H.S. Gupta, Bone matrix development in steroid-induced osteoporosis
762 is associated with a consistently reduced fibrillar stiffness linked to altered bone mineral quality, *Acta*
763 *Biomater* 76 (2018) 295-307.
- 764 [16] P.J. Thurner, C.G. Chen, S. Ionova-Martin, L. Sun, A. Harman, A. Porter, J.W. Ager, 3rd, R.O. Ritchie, T.
765 Alliston, Osteopontin deficiency increases bone fragility but preserves bone mass, *Bone* 46(6) (2010) 1564-
766 73.
- 767 [17] T.P. Van Staa, R.F. Laan, I.P. Barton, S. Cohen, D.M. Reid, C. Cooper, Bone density threshold and other
768 predictors of vertebral fracture in patients receiving oral glucocorticoid therapy, *Arthritis and rheumatism*
769 48(11) (2003) 3224-9.
- 770 [18] J. Compston, Management of glucocorticoid-induced osteoporosis, *Nature Reviews Rheumatology* 6(2)
771 (2010) 82-88.
- 772 [19] F. Mirza, E. Canalis, Secondary osteoporosis: Pathophysiology and management, *European Journal of*
773 *Endocrinology* 173(3) (2015) R131-R151.
- 774 [20] R. Rizzoli, E. Biver, Glucocorticoid-induced osteoporosis: Who to treat with what agent?, *Nature Reviews*
775 *Rheumatology* 11(2) (2015) 98-109.
- 776 [21] A.L. Boskey, E. DiCarlo, E. Paschalis, P. West, R. Mendelsohn, Comparison of mineral quality and quantity
777 in iliac crest biopsies from high- and low-turnover osteoporosis: an FT-IR microspectroscopic investigation,
778 *Osteoporosis Int* 16(12) (2005) 2031-2038.

779 [22] W.J. Landis, An overview of vertebrate mineralization with emphasis on collagen-mineral interaction,
780 Gravitational and space biology bulletin : publication of the American Society for Gravitational and Space
781 Biology 12(2) (1999) 15-26.

782 [23] E. Canalis, G. Mazziotti, A. Giustina, J.P. Bilezikian, Glucocorticoid-induced osteoporosis:
783 pathophysiology and therapy, *Osteoporosis Int* 18(10) (2007) 1319-1328.

784 [24] R.C. Pereira, A.M. Delany, E. Canalis, Effects of cortisol and bone morphogenetic protein-2 on stromal
785 cell differentiation: correlation with CCAAT-enhancer binding protein expression, *Bone* 30(5) (2002) 685-91.

786 [25] V. Krishnan, H.U. Bryant, O.A. MacDougald, Regulation of bone mass by Wnt signaling, *Journal of Clinical*
787 *Investigation* 116(5) (2006) 1202-1209.

788 [26] E. Canalis, Wnt signalling in osteoporosis: mechanisms and novel therapeutic approaches, *Nature*
789 *reviews. Endocrinology* 9(10) (2013) 575-83.

790 [27] D. Jia, C.A. O'Brien, S.A. Stewart, S.C. Manolagas, R.S. Weinstein, Glucocorticoids act directly on
791 osteoclasts to increase their life span and reduce bone density, *Endocrinology* 147(12) (2006) 5592-5599.

792 [28] H.J. Kim, H.B. Zhao, H. Kitaura, S. Bhattacharyya, J.A. Brewer, L.J. Muglia, F.P. Ross, S.L. Teitelbaum,
793 Glucocorticoids suppress bone formation via the osteoclast, *Journal of Clinical Investigation* 116(8) (2006)
794 2152-2160.

795 [29] P. Orcel, Updated recommendations on the management of glucocorticoid-induced osteoporosis, *Joint*
796 *Bone Spine* 81(6) (2014) 465-468.

797 [30] K. Hayashi, M. Yamamoto, Y. Murakawa, M. Yamauchi, H. Kaji, T. Yamaguchi, T. Sugimoto, Bone fragility
798 in male glucocorticoid-induced osteoporosis is not defined by bone mineral density, *Osteoporosis Int* 20(11)
799 (2009) 1889-1894.

800 [31] N.E. Lane, W. Yao, M. Balooch, R.K. Nalla, G. Balooch, S. Habelitz, J.H. Kinney, L.F. Bonewald,
801 Glucocorticoid-treated mice have localized changes in trabecular bone material properties and osteocyte
802 lacunar size that are not observed in placebo-treated or estrogen-deficient mice, *J Bone Miner Res* 21(3)
803 (2006) 466-476.

804 [32] R.S. Weinstein, D. Jia, C.C. Powers, S.A. Stewart, R.L. Jilka, A.M. Parfitt, S.C. Manolagas, The skeletal
805 effects of glucocorticoid excess override those of orchidectomy in mice, *Endocrinology* 145(4) (2004) 1980-7.

806 [33] A. Karunaratne, L. Xi, L. Bentley, D. Sykes, A. Boyde, C.T. Esapa, N.J. Terrill, S.D.M. Brown, R.D. Cox, R.V.
807 Thakker, H.S. Gupta, Multiscale alterations in bone matrix quality increased fragility in steroid induced
808 osteoporosis, *Bone* 84 (2016) 15-24.

809 [34] S.L. Greenspan, A. Wyman, F.H. Hooven, S. Adami, S. Gehlbach, F.A. Anderson Jr, S. Boone, A.Z. Lacroix,
810 R. Lindsay, J. Coen Netelenbos, Predictors of treatment with osteoporosis medications after recent fragility
811 fractures in a multinational cohort of postmenopausal women, *Journal of the American Geriatrics Society*
812 60(3) (2012) 455-461.

813 [35] V. Elliot-Gibson, E. Bogoch, S. Jamal, D. Beaton, Practice patterns in the diagnosis and treatment of
814 osteoporosis after a fragility fracture: a systematic review, *Osteoporosis Int* 15(10) (2004) 767-778.

815 [36] H. Gupta, S. Krauss, M. Kerschnitzki, A. Karunaratne, J. Dunlop, A. Barber, P. Boesecke, S. Funari, P.
816 Fratzl, Intrafibrillar plasticity through mineral/collagen sliding is the dominant mechanism for the extreme
817 toughness of antler bone, *Journal of the Mechanical Behavior of Biomedical Materials* 28 (2013) 366-382.

818 [37] H.S. Gupta, J. Seto, W. Wagermaier, P. Zaslansky, P. Boesecke, P. Fratzl, Cooperative deformation of
819 mineral and collagen in bone at the nanoscale, *Proceedings of the National Academy of Sciences of the*
820 *United States of America* 103(47) (2006) 17741-6.

821 [38] E.A. Zimmermann, B. Gludovatz, E. Schaible, B. Busse, R.O. Ritchie, Fracture resistance of human cortical
822 bone across multiple length-scales at physiological strain rates, *Biomaterials* 35(21) (2014) 5472-5481.

823 [39] L. Bentley, C.T. Esapa, M.A. Nesbit, R.A. Head, H. Evans, D. Lath, C.L. Scudamore, T.A. Hough, C. Podrini,
824 F.M. Hannan, W.D. Fraser, P.I. Croucher, M.A. Brown, S.D.M. Brown, R.D. Cox, R.V. Thakker, An N-ethyl-n-
825 nitrosourea induced corticotropin-releasing hormone promoter mutation provides a mouse model for
826 endogenous glucocorticoid excess, *Endocrinology* 155(3) (2014) 908-922.

827 [40] M. Toth, A. Grossman, Glucocorticoid-induced osteoporosis: lessons from Cushing's syndrome, *Clin*
828 *Endocrinol* 79(1) (2013) 1-11.

829 [41] I. Jager, P. Fratzl, Mineralized collagen fibrils: A mechanical model with a staggered arrangement of
830 mineral particles, *Biophysical Journal* 79(4) (2000) 1737-1746.

831 [42] A. Karunaratne, C.R. Esapa, J. Hiller, A. Boyde, R. Head, J.H. Bassett, N.J. Terrill, G.R. Williams, M.A.
832 Brown, P.I. Croucher, S.D. Brown, R.D. Cox, A.H. Barber, R.V. Thakker, H.S. Gupta, Significant deterioration in
833 nanomechanical quality occurs through incomplete extrafibrillar mineralization in rachitic bone: evidence
834 from in-situ synchrotron X-ray scattering and backscattered electron imaging, *J Bone Miner Res* 27(4) (2012)
835 876-90.

836 [43] A. Karunaratne, A. Boyde, C.T. Esapa, J. Hiller, N.J. Terrill, S.D. Brown, R.D. Cox, R.V. Thakker, H.S. Gupta,
837 Symmetrically reduced stiffness and increased extensibility in compression and tension at the mineralized
838 fibrillar level in rachitic bone, *Bone* (2012).

839 [44] H.D. Barth, M.E. Launey, A.A. Macdowell, J.W. Ager, 3rd, R.O. Ritchie, On the effect of X-ray irradiation
840 on the deformation and fracture behavior of human cortical bone, *Bone* 46(6) (2010) 1475-85.

841 [45] H.S. Gupta, J. Seto, W. Wagermaier, P. Zaslansky, P. Boesecke, P. Fratzl, Cooperative deformation of
842 mineral and collagen in bone at the nanoscale, *Proceedings of the National Academy of Sciences of the*
843 *United States of America* 103(47) (2006) 17741-6.

844 [46] H.S. Gupta, W. Wagermaier, G.a. Zickler, D. Raz-Ben Aroush, S.S. Funari, P. Roschger, H.D. Wagner, P.
845 Fratzl, Nanoscale deformation mechanisms in bone, *Nano Letters* 5(10) (2005) 2108-11.

846 [47] W.J. Landis, K.J. Hodgens, J. Arena, M.J. Song, B.F. McEwen, Structural relations between collagen and
847 mineral in bone as determined by high voltage electron microscopic tomography, *Microscopy research and*
848 *technique* 33(2) (1996) 192-202.

849 [48] M. Basham, J. Filik, M.T. Wharmby, P.C. Chang, B. El Kassaby, M. Gerring, J. Aishima, K. Levik, B.C.
850 Pulford, I. Sikharulidze, *Data Analysis Workbench (DAWN)*, *Journal of Synchrotron Radiation* 22(3) (2015)
851 853-858.

852 [49] A. Karunaratne, C.R. Esapa, J. Hiller, A. Boyde, R. Head, J.H. Bassett, N.J. Terrill, G.R. Williams, M.A.
853 Brown, P.I. Croucher, S.D. Brown, R.D. Cox, A.H. Barber, R.V. Thakker, H.S. Gupta, Significant deterioration in
854 nanomechanical quality occurs through incomplete extrafibrillar mineralization in rachitic bone: evidence
855 from in-situ synchrotron X-ray scattering and backscattered electron imaging, *Journal of bone and mineral*
856 *research : the official journal of the American Society for Bone and Mineral Research* 27(4) (2012) 876-90.

857 [50] M.J. Berger, J.H. Hubbell, S.M. Seltzer, J. Chang, J.S. Coursey, R. Sukumar, D.S. Zucker, K. Olsen, *XCOM:*
858 *Photon Cross Section Database*, 2010.

859 [51] I. Zizak, P. Roschger, O. Paris, B.M. Misof, A. Berzlanovich, S. Bernstorff, H. Amenitsch, K. Klaushofer, P.
860 Fratzl, Characteristics of mineral particles in the human bone/cartilage interface, *J Struct Biol* 141(3) (2003)
861 208-17.

862 [52] H.S. Gupta, S. Schratte, W. Tesch, P. Roschger, A. Berzlanovich, T. Schoeberl, K. Klaushofer, P. Fratzl,
863 Two different correlations between nanoindentation modulus and mineral content in the bone-cartilage
864 interface, *J Struct Biol* 149(2) (2005) 138-48.

865 [53] D. Planchard, *SOLIDWORKS 2017 Reference Guide*, SDC Publications 2017.

866 [54] Hibbett, Karlsson, Sorensen, *ABAQUS/standard: User's Manual*, Hibbett, Karlsson & Sorensen 1998.

867 [55] H.J. Gao, B.H. Ji, I.L. Jager, E. Arzt, P. Fratzl, Materials become insensitive to flaws at nanoscale: Lessons
868 from nature, *Proceedings of the National Academy of Sciences of the United States of America* 100(10)
869 (2003) 5597-5600.

870 [56] B. Ji, H. Gao, Elastic properties of nanocomposite structure of bone, *Composites Science and Technology*
871 66(9) (2006) 1209-1215.

872 [57] B. Bar-On, H.D. Wagner, Mechanical model for staggered bio-structure, *Journal of the Mechanics and*
873 *Physics of Solids* 59(9) (2011) 1685-1701.

874 [58] T.K. Hight, J.F. Brandeau, Mathematical-Modeling of the Stress-Strain Strain Rate Behavior of Bone
875 Using the Ramberg-Osgood Equation, *Journal of Biomechanics* 16(6) (1983) 445-450.

876 [59] W. Yang, V.R. Sherman, B. Gludovatz, E. Schaible, P. Stewart, R.O. Ritchie, M.A. Meyers, On the tear
877 resistance of skin, *Nature Communications* 6 (2015) 6649.

878 [60] W.H. Press, S.A. Teukolsky, W.T. Vetterling, B.P. Flannery, *Numerical recipes 3rd edition: The art of*
879 *scientific computing*, Cambridge university press 2007.

880 [61] A. Vercher, E. Giner, C. Arango, J.E. Tarancón, F.J. Fuenmayor, Homogenized stiffness matrices for
881 mineralized collagen fibrils and lamellar bone using unit cell finite element models, *Biomechanics and*
882 *Modelling in Mechanobiology* 13(2) (2014) 437-449.

883 [62] A. Ural, P. Zioupos, D. Buchanan, D. Vashishth, The effect of strain rate on fracture toughness of human
884 cortical bone: A finite element study, *Journal of the Mechanical Behavior of Biomedical Materials* 4(7) (2011)
885 1021-1032.

886 [63] S. Charoenphan, A. Polchai, Finite element modeling for strain rate dependency of fracture resistance in
887 compact bone, *J Biomech Eng* 129(1) (2007) 20-5.

888 [64] U. Hansen, P. Zioupos, R. Simpson, J.D. Currey, D. Hynd, The effect of strain rate on the mechanical
889 properties of human cortical bone, *Journal of biomechanical engineering* 130(1) (2008) 011011.

890 [65] Z. Asgharpour, P. Zioupos, M. Graw, S. Peldschus, Development of a strain rate dependent material
891 model of human cortical bone for computer-aided reconstruction of injury mechanisms, *Forensic Sci Int* 236
892 (2014) 109-16.

893 [66] T.P.M. Johnson, S. Socrate, M.C. Boyce, A viscoelastic, viscoplastic model of cortical bone valid at low
894 and high strain rates, *Acta Biomater* 6(10) (2010) 4073-4080.

895 [67] A.C. Deymier-Black, F. Yuan, A. Singhal, J.D. Almer, L.C. Brinson, D.C. Dunand, Evolution of load transfer
896 between hydroxyapatite and collagen during creep deformation of bone, *Acta Biomater* 8(1) (2012) 253-61.

897 [68] J. Akbarzadeh, S. Puchegger, A. Stojanovic, H.O.K. Kirchner, W.H. Binder, S. Bernstorff, P. Zioupos, H.
898 Peterlik, Timescales of self-healing in human bone tissue and polymeric ionic liquids, *Bioinspired, Biomimetic*
899 *and Nanobiomaterials* 3(3) (2014) 123-130.

900 [69] D. Lau, O. Büyükköztürk, M.J. Buehler, Multiscale modeling of organic-inorganic interface: From
901 molecular dynamics simulation to finite element modeling, *Materials Research Society Symposium*
902 *Proceedings*, 2012, pp. 44-49.

903 [70] J.P.R.O. Orgel, T.C. Irving, A. Miller, T.J. Wess, Microfibrillar structure of type I collagen in situ,
904 *Proceedings of the National Academy of Sciences* 103(24) (2006) 9001.

905 [71] M. Liebi, M. Georgiadis, A. Menzel, P. Schneider, J. Kohlbrecher, O. Bunk, M. Guizar-Sicairos,
906 Nanostructure surveys of macroscopic specimens by small-angle scattering tensor tomography, *Nature*
907 527(7578) (2015) 349-+.

908 [72] M. Qwamizadeh, Z. Zhang, K. Zhou, Y.W. Zhang, On the relationship between the dynamic behavior and
909 nanoscale staggered structure of the bone, *Journal of the Mechanics and Physics of Solids* 78 (2015) 17-31.

910 [73] M.-M. Giraud-Guille, Plywood structures in nature, *Current Opinion in Solid State and Materials Science*
911 3(3) (1998) 221-227.

912 [74] M.J. Turunen, J.D. Kaspersen, U. Olsson, M. Guizar-Sicairos, M. Bech, F. Schaff, M. Tägil, J.S. Jurvelin, H.
913 Isaksson, Bone mineral crystal size and organization vary across mature rat bone cortex, *Journal of Structural*
914 *Biology* 195(3) (2016) 337-344.

915 [75] A.A. Poundarik, T. Diab, G.E. Sroga, A. Ural, A.L. Boskey, C.M. Gundberg, D. Vashishth, Dilatational band
916 formation in bone, *Proceedings of the National Academy of Sciences of the United States of America* 109(47)
917 (2012) 19178-83.

918 [76] T. Hassenkam, G.E. Fantner, J.A. Cutroni, J.C. Weaver, D.E. Morse, P.K. Hansma, High-resolution AFM
919 imaging of intact and fractured trabecular bone, *Bone* 35(1) (2004) 4-10.

920 [77] Y. Wang, S. Von Euw, G. Laurent, C. Crevant, L. Bonhomme-Coury, M.M. Giraud-Guille, F. Babonneau, N.
921 Nassif, T. Azais, Impact of collagen confinement vs. ionic substitutions on the local disorder in bone and
922 biomimetic apatites, *Mater Horizons* 1(2) (2014) 224-231.

923 [78] W.Y. Ching, P. Rulis, A. Misra, Ab initio elastic properties and tensile strength of crystalline
924 hydroxyapatite, *Acta Biomater* 5(8) (2009) 3067-3075.

925 [79] Y. Bouligand, Twisted fibrous arrangements in biological materials and cholesteric mesophases, *Tissue*
926 *and Cell* 4(2) (1972) 189-217.

927